



Publication Year	2016
Acceptance in OA	2020-12-29T14:07:44Z
Title	Thermodynamic perturbations in the X-ray halo of 33 clusters of galaxies observed with Chandra ACIS
Authors	Hofmann, F., Sanders, J. S., Nandra, K., Clerc, N., GASPARI, MASSIMO
Publisher's version (DOI)	10.1051/0004-6361/201526925
Handle	http://hdl.handle.net/20.500.12386/29289
Journal	ASTRONOMY & ASTROPHYSICS
Volume	585

Thermodynamic perturbations in the X-ray halo of 33 clusters of galaxies observed with *Chandra* ACIS[★]

F. Hofmann¹, J. S. Sanders¹, K. Nandra¹, N. Clerc¹, and M. Gaspari^{2,3,★★}

¹ Max-Planck-Institut für extraterrestrische Physik, Giessenbachstraße, 85748 Garching, Germany
e-mail: fhofmann@mpe.mpg.de

² Department of Astrophysical Sciences, Princeton University, Princeton, NJ 08544, USA

³ Max-Planck-Institut für Astrophysik, Karl-Schwarzschildstraße, 85748 Garching, Germany

Received 9 July 2015 / Accepted 27 October 2015

ABSTRACT

Context. In high-resolution X-ray observations of the hot plasma in clusters of galaxies, significant structures caused by AGN feedback, mergers, and turbulence can be detected. Many clusters have been observed by *Chandra* in great depth and at high resolution.

Aims. With the use of archival data taken with the *Chandra* ACIS instrument, the aim was to study thermodynamic perturbations of the X-ray emitting plasma and to apply this to better understand the thermodynamic and dynamic state of the intracluster medium (ICM).

Methods. We analysed deep observations for a sample of 33 clusters with more than 100 ks of *Chandra* exposure each at distances between redshift 0.025 and 0.45. The combined exposure of the sample is 8 Ms. Fitting emission models to different regions of the extended X-ray emission, we searched for perturbations in density, temperature, pressure, and entropy of the hot plasma.

Results. For individual clusters, we mapped the thermodynamic properties of the ICM and measured their spread in circular concentric annuli. Comparing the spread of different gas quantities to high-resolution 3D hydrodynamic simulations, we constrained the average Mach number regime of the sample to $\text{Mach}_{\text{ID}} \approx 0.16 \pm 0.07$. In addition we found a tight correlation between metallicity, temperature, and redshift with an average metallicity of $Z \approx 0.3 \pm 0.1 Z_{\odot}$.

Conclusions. This study provides detailed perturbation measurements for a large sample of clusters that can be used to study turbulence and make predictions for future X-ray observatories like eROSITA, Astro-H, and Athena.

Key words. galaxies: clusters: general – X-rays: galaxies: clusters – turbulence

1. Introduction

In the current picture of the evolution of the universe, clusters of galaxies have formed in the deep potential wells created by clumping of dark matter (DM) around remnant density fluctuations after the Big Bang. The majority of the mass in clusters is made of DM, which is only observed indirectly through its gravitational effects. The second component of clusters is baryonic matter consisting mainly of very thin hot plasma (the intracluster medium, ICM), heated by the gravitational accretion into the potential wells, and emitting strongest in X-ray wavelength because of its high temperatures. The smallest fraction of the mass is in the stellar content of the clustered galaxies, which is observable in visible light. The behaviour of DM in the cluster potential is believed to be well understood from cosmological simulations (e.g. Springel et al. 2005) and observations of gravitational lensing effects on visible light (Broadhurst et al. 1995; Kaiser et al. 1995; Allen et al. 2002; Bradač et al. 2006; Zhang et al. 2008; Mahdavi et al. 2013). The member galaxies of a cluster are well described as collisionless particles moving in the cluster potential by measuring the line-of-sight velocity dispersion

in the optical (see e.g. Zhang et al. 2011; Rines et al. 2013). The complex dynamic and thermodynamic processes in the hot ICM can be studied with X-ray observations. Other phases of the ICM have been studied at different wavelength with UV and H α (e.g. McDonald et al. 2011) or radio observations (e.g. Dolag et al. 2001; Govoni et al. 2004).

Schuecker et al. (2004) first related fluctuations in the projected pressure maps of the hot, X-ray emitting, ICM of the Coma cluster to turbulence. Turbulence has been discussed as a significant heating mechanism (see Dennis & Chandran 2005; Ruzkowski & Oh 2010; Gaspari et al. 2012a), which is important to understand the heating and cooling balance (see cooling flow problem; Fabian 1994) in clusters and to estimate the amount of non-thermal pressure support (see e.g. simulations by Nelson et al. 2014). Zhuravleva et al. (2014) recently studied turbulence in the Perseus and Virgo cluster by analysing fluctuations in the surface brightness of the cluster emission. Asymmetries and fluctuations within thermodynamic properties of the hot plasma can be used to estimate the amount of turbulence (e.g. Gaspari & Churazov 2013; Gaspari et al. 2014). This has been studied in the PKS 0745-191 galaxy cluster by Sanders et al. (2014). We applied a similar technique to the current sample of 33 clusters and compared our results to the findings of cluster simulations (e.g. Vazza et al. 2009; Lau et al. 2009).

The amount of turbulence in the hot ICM is hard to directly measure. Simulations of galaxy clusters predict turbulent

* Tables 2–67 are only available at the CDS via anonymous ftp to cdsarc.u-strasbg.fr (130.79.128.5) or via <http://cdsarc.u-strasbg.fr/viz-bin/qcat?J/A+A/585/A130>

** Einstein and Spitzer Fellow

motions of several hundreds of km s^{-1} (e.g. Dolag et al. 2005; Nelson et al. 2014; Gaspari et al. 2014). Sanders et al. (2011), Sanders & Fabian (2013), and Pinto et al. (2015) were able to obtain upper limits on the velocity broadening of spectra for a large sample of clusters. However current X-ray instruments only provide the spectral resolution needed to detect significant broadening due to turbulence in a few possible cases.

The basis for this study was the X-ray all-sky survey of the ROSAT mission (1990 to 1999; see Truemper 1982). The clusters identified in this survey (e.g. Böhringer et al. 2000, 2004) were followed up with the current generation X-ray telescopes *Chandra*, *XMM-Newton*, and *Suzaku*. For the substructure study we used observations of ROSAT clusters with the X-ray observatory on board the *Chandra* satellite, which delivers the best spatial and very good spectral resolution. Since its launch in 1999, *Chandra* has frequently been used to study clusters of galaxies as individual systems and as cosmological probes (e.g. Allen et al. 2004, 2008; Vikhlinin et al. 2009b,a). The telescope’s high resolution showed an unexpected complexity of the ICM structure in many cases (e.g. Fabian et al. 2000; McNamara et al. 2000; Markevitch et al. 2000, 2002; Sanders et al. 2005; Fabian et al. 2006; Forman et al. 2007). We analysed a sample of clusters and mapped their thermodynamic properties based on the large archive of deep cluster observations. We specifically investigated perturbations in the thermodynamic parameters of the ICM, which according to recent high-resolution simulations can be used to trace turbulence in the ICM via the normalisation of the ICM power spectrum (e.g. in density; Gaspari et al. 2014). By measuring the slope of the power spectrum, we can constrain the main transport processes in the hot ICM, such as thermal conductivity (Gaspari & Churazov 2013).

The paper is structured as follows: Sect. 2 describes the sample selection and data reduction; Sect. 3 describes the analysis of perturbations; in Sect. 4 the main results are presented; Sect. 5 contains results for individual systems; in Sect. 6 the findings are discussed; and Sect. 7 contains the conclusions.

For all our analysis we used a standard Λ CDM cosmology with $H_0 = 71 \text{ km s}^{-1} \text{ Mpc}^{-1}$, $\Omega_M = 0.27$ and $\Omega_\Lambda = 0.73$ and relative solar abundances as given by Anders & Grevesse (1989).

2. Observations and data reduction

We used archival observations with the *Chandra* Advanced CCD Imaging Spectrometer (ACIS; Garmire et al. 2003) using the imaging (-I) or spectral (-S) CCD array (about 0.1 to 10 keV energy range). This instrument provides high spatial ($\sim 1''$) and spectral resolution ($\sim 100 \text{ eV}$ full width half maximum, FWHM). The field of view (FOV) is limited, so that only the inner $5\text{--}10'$ of any cluster are homogeneously covered. See Sect. A for a list of all analysed clusters and their individual exposure times.

2.1. Sample selection

We based our sample selection on the NORAS (378 sources; see Böhringer et al. 2000), REFLEX (447 sources, see Böhringer et al. 2004), and CIZA (73 sources; see Ebeling et al. 2002) catalogues. They all have been derived from ROSAT observations, which deliver the only true imaging all-sky X-ray survey to date. The NORAS and REFLEX catalogues cover the regions north and south of the Galactic plane ($\pm 20^\circ$), excluding the Magellanic Clouds. The CIZA sample covers the Galactic plane and thus adds some interesting clusters to our sample. However in the Galactic plane we have to deal with higher foreground absorption of X-rays (due to the column density n_{H} of the Galaxy).

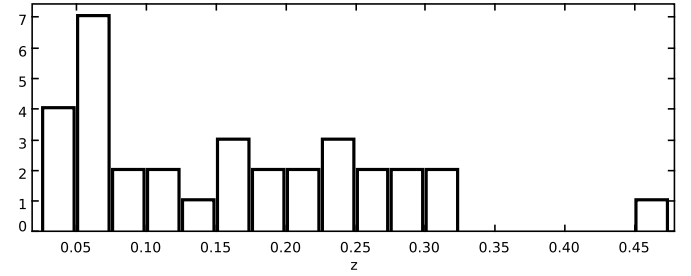


Fig. 1. Histogram of the redshift (z) distribution of the final sample of 33 clusters.

Not all of these clusters have been observed with *Chandra*, but the predominantly X-ray bright clusters in which the structure of the ICM could be well studied have been observed with *Chandra*. We matched all *Chandra* ACIS observations available from the *Chandra* Data Archive (CDA¹ on 2013-10-09) with cluster positions in the ROSAT catalogues mentioned above.

We set a luminosity cut on the ~ 300 clusters correlated with *Chandra* observations, and only added clusters to the sample that had a luminosity of more than $2.0 \times 10^{44} \text{ erg/s}$ in the 0.1–2.4 keV ROSAT energy band. We only accepted clusters and groups of galaxies with a redshift of $z \geq 0.025$ to ensure all clusters fit reasonably well into the *Chandra* ACIS FOV. This excludes some nearby extended systems where larger radii are not homogeneously covered (e.g. the Coma cluster, see Vikhlinin et al. 2009b). After these selections we used all clusters with $\geq 100 \text{ ks}$ raw *Chandra* exposure time. Our final sample consists of 33 X-ray bright, massive, nearby clusters of galaxies. The velocity dispersion of galaxies in the clusters is around 1000 km s^{-1} for most systems. The cluster halo masses within the overdensity radius r_{500} range from $1 \times 10^{14} M_\odot$ to $2 \times 10^{15} M_\odot$ (Table 1). At r_{500} the average density of the cluster is 500 times the critical density of the universe at the cluster redshift. The luminosity range is $(2\text{--}63) \times 10^{44} \text{ erg/s}$ (0.1–2.4 keV X-ray luminosity, see Tables A.1–A.3), the redshift ranges from 0.025 to 0.45 (see Fig. 1), and the total exposure analysed in this work is $\sim 8 \text{ Ms}$ (corresponding to more than 90 days of observations). For a list of observations used in this study, see Table B.1.

2.2. Cluster maps

For the *Chandra* data reduction we used a pipeline of various *Python* and *C++* scripts to accurately map the structure of the ICM. The pipeline downloads all relevant datasets from the *Chandra* data archive (CDA) and reprocesses them using the *Chandra* standard data processing (SDP) with the *Chandra* Interactive Analysis of Observations software package (CIAO; Fruscione et al. 2006) version 4.5 and the *Chandra* Calibration Database (CalDB; Graessle et al. 2007) version 4.5.9.

A background light curve for each observation is created and times of high background are removed from the event files by iteratively removing times where the count rate is more than 3σ from the median of the light curve. Via the CIAO tool `acis_bkgrnd_lookup`, we find a suitable blank-sky background file, which is provided by the *Chandra* X-ray centre (see e.g. Markevitch et al. 2003) and derive the background in each of the cluster observations. We correct residual spatial offsets between the individual observations, if necessary, by detecting point sources in each image with `wavdetect` and correlating the individual detection lists. Offsets in other event files

¹ <http://cxc.harvard.edu/cda/>

Table 1. Sample properties.

Cluster ^a	Abbrev. ^a	n_{H} [10^{22} cm^{-2}]	$\langle T \text{ map} \rangle$ [keV]	r_{FOV}^b [Mpc]	r_{500}^c [Mpc]	M_{500}^c [$10^{14} M_{\odot}$]	r_{FOV}/r_{500}
RX J1347-114	rxj1347	0.046	14.7 ± 0.125	0.48	1.57 ± 0.05	17.7 ± 1.8	0.31
1E 0657-56	1e0657	0.049	12.6 ± 0.112	0.98	1.58 ± 0.06	15.3 ± 1.9	0.62
A 2390	a2390	0.062	10.8 ± 0.104	0.55	1.51 ± 0.07	12.4 ± 1.8	0.36
A 1689	a1689	0.018	10.4 ± 0.115	0.41	1.52 ± 0.07	12.1 ± 1.8	0.27
A 401	a401	0.099	8.6 ± 0.071	0.36	1.45 ± 0.09	9.5 ± 1.7	0.25
A 2204	a2204	0.057	8.5 ± 0.035	0.42	1.39 ± 0.08	9.0 ± 1.6	0.30
A 2034	a2034	0.015	8.3 ± 0.107	0.31	1.40 ± 0.09	8.8 ± 1.6	0.22
A 1413	a1413	0.018	8.3 ± 0.107	0.36	1.38 ± 0.08	8.7 ± 1.6	0.26
A 2744	a2744	0.014	8.7 ± 0.229	1.09	1.30 ± 0.08	8.6 ± 1.5	0.84
A 1835	a1835	0.020	8.5 ± 0.040	0.42	1.32 ± 0.08	8.5 ± 1.5	0.32
PKS 0745-191	pks0745	0.373	7.9 ± 0.031	0.40	1.37 ± 0.09	8.2 ± 1.6	0.29
A 665	a665	0.043	7.3 ± 0.137	0.48	1.26 ± 0.09	6.9 ± 1.5	0.38
CYGNUS A	cygnusa	0.272	6.9 ± 0.022	0.29	1.30 ± 0.10	6.8 ± 1.5	0.22
ZW 3146	zw3146	0.025	7.0 ± 0.064	0.39	1.18 ± 0.09	6.3 ± 1.4	0.33
A 520	a520	0.057	6.7 ± 0.073	0.79	1.20 ± 0.09	6.1 ± 1.4	0.66
A 1795	a1795	0.012	6.2 ± 0.008	0.30	1.23 ± 0.10	5.8 ± 1.4	0.24
A 1650	a1650	0.013	6.0 ± 0.036	0.28	1.20 ± 0.10	5.5 ± 1.4	0.23
A 3667	a3667	0.044	5.8 ± 0.025	0.37	1.20 ± 0.10	5.3 ± 1.4	0.31
A 907	a907	0.054	5.8 ± 0.061	0.28	1.14 ± 0.10	5.0 ± 1.3	0.24
A 521	a521	0.049	5.9 ± 0.177	0.54	1.10 ± 0.10	4.8 ± 1.3	0.49
A 1995	a1995	0.012	5.9 ± 0.173	0.31	1.06 ± 0.09	4.7 ± 1.2	0.29
A 2146	a2146	0.030	5.7 ± 0.031	0.50	1.08 ± 0.10	4.6 ± 1.2	0.46
MS0735.6+7421	ms0735	0.033	5.5 ± 0.030	0.30	1.08 ± 0.10	4.5 ± 1.2	0.28
MS 1455.0+2232	ms1455	0.032	5.1 ± 0.055	0.31	1.01 ± 0.10	3.9 ± 1.2	0.30
A 2199	a2199	0.009	4.4 ± 0.010	0.19	1.05 ± 0.12	3.5 ± 1.2	0.18
A 496	a496	0.038	4.3 ± 0.012	0.20	1.04 ± 0.12	3.4 ± 1.2	0.19
A 2597	a2597	0.025	4.0 ± 0.014	0.21	0.98 ± 0.12	2.9 ± 1.1	0.21
3C348 (HERCULES A)	3c348	0.062	3.9 ± 0.032	0.23	0.94 ± 0.12	2.7 ± 1.1	0.25
A 1775	a1775	0.010	3.7 ± 0.047	0.22	0.94 ± 0.13	2.6 ± 1.1	0.23
HYDRA A	hydraa	0.047	3.5 ± 0.009	0.22	0.93 ± 0.13	2.4 ± 1.1	0.23
2A 0335+096	2a0335	0.175	2.9 ± 0.005	0.18	0.84 ± 0.15	1.8 ± 1.0	0.21
SERSIC 159-03	seraic159	0.011	2.8 ± 0.012	0.17	0.82 ± 0.15	1.7 ± 0.9	0.20
A 2052	a2052	0.027	2.3 ± 0.002	0.15	0.76 ± 0.17	1.3 ± 0.9	0.19

Notes. ^(a) Most commonly used cluster name and abbreviated catalogue names of clusters (compare to Tables A.1–A.3). Sorted on descending mass (M_{500}). ^(b) Maximum radius (from X-ray peak) covered in our analysis. ^(c) Overdensity radii r_{500} and M_{500} were calculated using the mass-temperature scaling relation from Vikhlinin et al. (2009a) for an estimate on the r_{500} fraction covered in each object. We used $\langle T \text{ map} \rangle$ as input for the scaling relation and estimated errors assuming a 0.5 keV systematic uncertainty (see scatter in Fig. 4).

are corrected by updating their aspect solution, using the deepest observation as a reference. With this procedure we ensure the best resolution of small-scale ICM variations. We create images from the event file of each dataset using an energy range of 0.5 keV to 7.0 keV and binning the image by a factor of two (1 pix $\sim 0.98''$). For each image, an exposure-map is created for an energy of 1.5 keV. After the analysis of the individual observations, all images, background, and exposure maps are merged. A second point source detection with wavdetect is run on the merged images and, after carefully screening the detection list, the point sources are masked from the image. In the following steps, the image is adaptively smoothed with $snsmooth = 15$ and then binned into regions of equal signal-to-noise ratio (S/N) of 50 (>2500 counts per bin) with the contour binning technique `contbin` (see Sanders 2006).

For the asymmetry (i.e. spread) analysis (Sect. 3.1), we generated maps with $S/N = 25$ (>625 counts per bin) for clusters where we obtained less than 50 independent spatial-spectral bins from the $S/N = 50$ analysis. For each of the bins a detector response is calculated and the count spectrum extracted. Spectra of the same detectors are added together (ACIS-I and ACIS-S separately) and fitted using C-Statistics in XSPEC

version 6.11 (Cash 1979; Arnaud 1996) with the `apec` model for collisionally-ionised diffuse gas, which is based on the ATOMDB code v2.0.2 (Foster et al. 2012). The fit was done using a fixed foreground column density (n_{H} [cm^{-2}], see Table 1), which is determined from the Leiden/Argentine/Bonn (LAB) survey of Galactic HI (based on Kalberla et al. 2005), and a fixed redshift from the ROSAT catalogues.

We only carried out the fit with n_{H} as a free parameter in the special case of PKS 0745-191 because of its location behind the Galactic plane and strong n_{H} variation within the FOV. The free parameters of the fit to the count spectrum are temperature T [keV], the metal abundance Z as a fraction of solar abundances (reference solar abundance Z_{\odot} from Anders & Grevesse 1989) and the normalisation η [$\text{cm}^{-5} \text{ arcsec}^{-2}$] of the fit, which is defined as

$$\eta = 10^{-14} / (4\pi D_A^2 (1+z)^2) \int n_e n_p dV, \quad (1)$$

where D_A is the angular diameter distance to the source, n_e and n_p the electron and hydrogen densities integrated over the volume V . Assuming a spherical source, uniform density, and full ionisation with 10 per cent helium and 90 per cent hydrogen abundance (i.e. $n_e \sim 1.2 n_p$), the hydrogen density can be

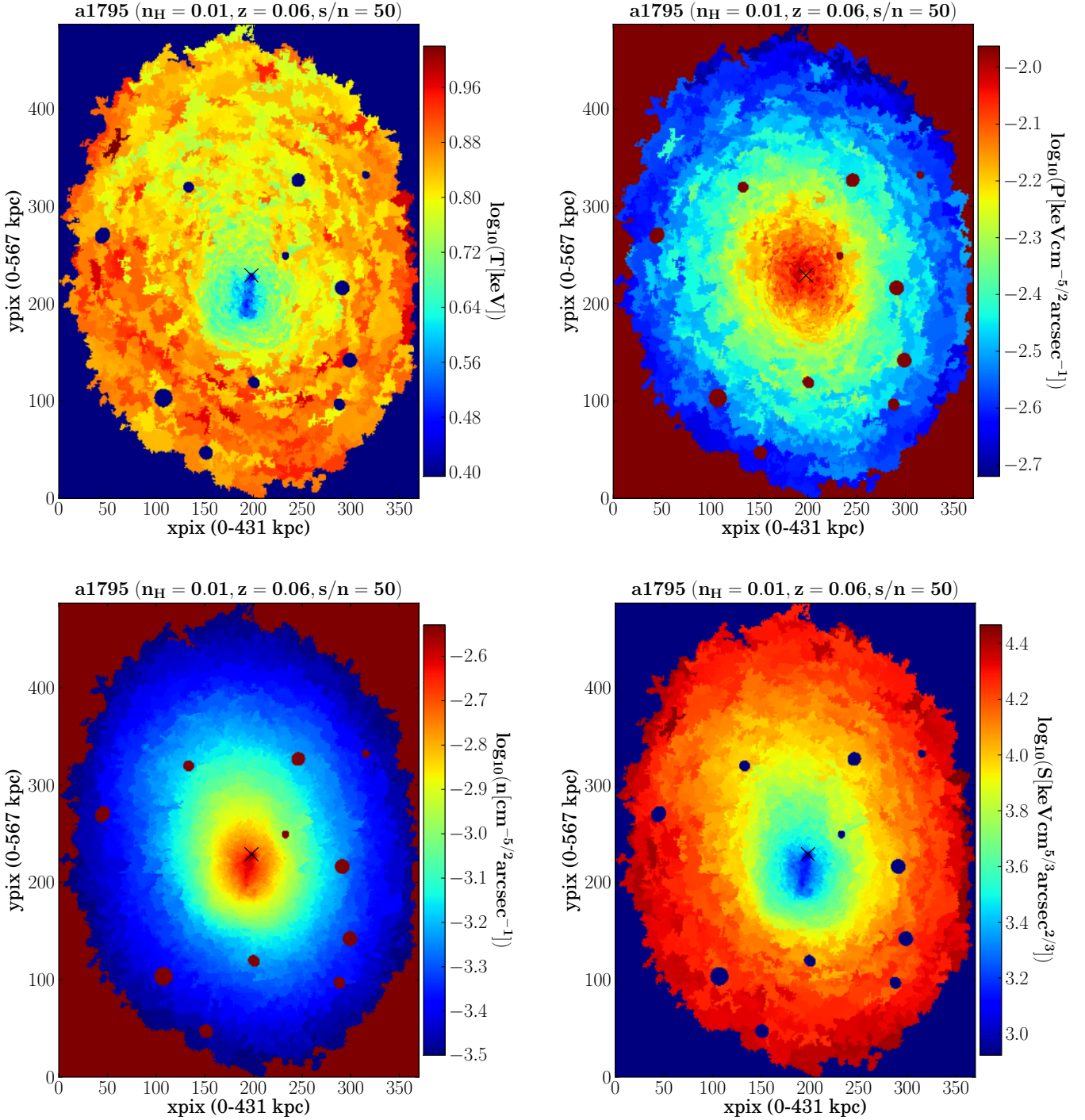


Fig. 2. From top left to bottom right: 2D maps of projected temperature, pressure, density, and entropy of A 1795. The cross denotes the X-ray peak and centre for profile analysis. Point sources and regions below the surface brightness cut are set to zero. xpix and ypix are pixels along RA and Dec direction and the overall range in kpc is given. Scale: 1 pix $\sim 1''$. The plot titles indicate the abbreviated cluster name, the average foreground column density n_{H} [cm^{-2}], and the redshift.

calculated as

$$n_{\text{p}} = \sqrt{\frac{(1+z)^2 10^{14} \eta}{1.2 \Theta^3 D_{\text{A}}}} \equiv \xi \cdot \sqrt{\eta}, \quad (2)$$

where Θ is the angular size of the source (see the ATOMDB webpage² for these equations). The factor ξ changes for different

² <http://atomdb.org/faq.php>

clusters and assumed geometries. We assumed $n_{\text{p}} \sim \sqrt{\eta}$ within any given cluster. The fit parameters of each bin are translated into images to obtain maps of the temperature, metal abundance, and normalisation of the ICM.

From the 2D maps of the spectral fitting, we calculated a projected pseudo-density, pressure, and entropy in each spatial bin of the ICM emission. We assumed a constant line-of-sight depth for all spectral regions calculating pseudo-density n as square

root of the fit normalisation, normalised by region size,

$$n \equiv \sqrt{\eta} \left[\text{cm}^{-5/2} \text{ arcsec}^{-1} \right], \quad (3)$$

pseudo-pressure as,

$$P \equiv n \times \text{temperature} \left[\text{keV cm}^{-5/2} \text{ arcsec}^{-1} \right], \quad (4)$$

and pseudo-entropy as,

$$S \equiv n^{-2/3} \times \text{temperature} \left[\text{keV cm}^{5/3} \text{ arcsec}^{2/3} \right]. \quad (5)$$

We adopted a common definition of entropy for galaxy cluster studies, which is related to the standard definition of thermodynamic entropy s through

$$s = k_B \ln \left(S^{3/2} (\mu m_p)^{5/2} \right) + s_0, \quad (6)$$

with mean particle mass μ and proton mass m_p (see e.g. Voit 2005). Relative cooling times of the ICM are proportional to $n^{-1} \times \text{temperature}^{1/2}$ [$\text{keV}^{1/2} \text{ cm}^{5/2} \text{ arcsec}$] where Bremsstrahlung emission dominates (see e.g. Sarazin 1986, and references therein).

All distances were calculated with the redshift given in the ROSAT cluster catalogues. All uncertainties are 1σ confidence intervals unless stated otherwise. All further analysis only includes regions where the area-normalised normalisation of the fit was above $10^{-7} \text{ cm}^{-5} \text{ arcsec}^{-2}$. This corresponds roughly to a surface brightness cut below in which there were insufficient counts for detailed spectral analysis. For an example refer to the maps of Abell 1795 in Fig. 2.

3. Analysis of perturbations

We were able to study the ICM in great detail for a large sample of clusters based on the very detailed spatial-spectral analysis of this sample of clusters with deep *Chandra* observations.

3.1. Asymmetry measurement

One of the main goals of this study was to better characterise the thermodynamic state of the ICM in individual clusters and to identify general trends in the whole sample. Important indicators of the state of the hot gas are fluctuations in thermodynamic properties. Gaspari & Churazov (2013) and Gaspari et al. (2014), in recent high-resolution simulations, have shown a connection between these kinds of fluctuations and the Mach number of gas motion in the ICM.

We examined the asymmetry (i.e. the spread) of thermodynamic properties in concentric, circular annuli of radius r around the peak X-ray emission. As input we used the S/N 50 ICM maps (see Sect. 2.2). For nine clusters (a907, ms1455, a521, a665, a2744, a1775, a1995, 3c348, zw3146), we used S/N 25 instead to obtain at least five radial spread bins with a minimum of five data points per bin for all clusters. Assuming the data points are scattered statistically as a result of their uncertainties σ_{stat} , we tested for intrinsic spread σ_{spread} in the radial profiles (see e.g. Fig. 3).

To avoid contamination of the spread measurement by the slope, we modelled the radial profile by interpolating between several nodes. This modelled average profile can be described by a function $\mu(r, \mu_1, \dots, \mu_N)$ with $N = 7$. The nodes divide the cluster profile into bins with equal number of data points. We used a minimum of five data points per model node and

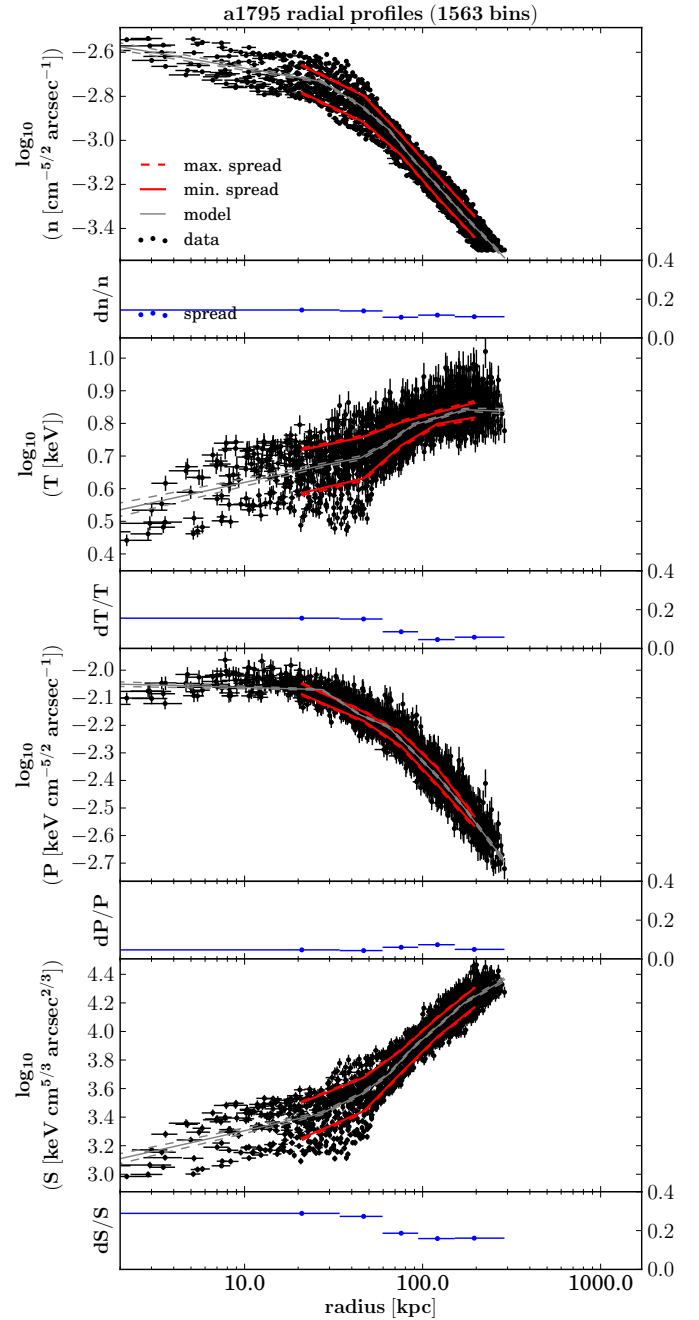


Fig. 3. Radial profiles of projected density, temperature, pressure, and entropy of A 1795. The centre is marked by a cross in Fig. 2. Error bars are the fit errors and the standard deviation of the radial distribution of the respective spatial-spectral bin. The plotted lines show limits on intrinsic scatter around an average seven-node model (grey lines) within the given radial range (see Sect. 3.1). The *small panels* show the measured fractional scatter ($M = 5$) with confidence and radial range.

if this criterion was not met we reduced the number of nodes. The intrinsic fractional spread is given by a function of the form $\sigma_{\text{spread}}(r, \sigma_{\text{spread},1}, \dots, \sigma_{\text{spread},M})$. We performed three independent spread measurements, splitting the profiles into one, two, and five radial bins ($M = 1, 2, 5$) to measure the spread in the clusters with different radial resolutions.

For every data point, we obtained the mean value $\mu(r_i)$ of the thermodynamic profile at its radius r_i by interpolating between the model nodes (see grey lines in Fig. 3). The individual spread

values of each data point $\sigma_{\text{spread}}(r_i)$ are constant within a given radial bin (see spread profile in Fig. 3).

The intrinsic spread of cluster properties was estimated using a Markov chain Monte Carlo (MCMC) method implemented with `emcee` (see [Foreman-Mackey et al. 2013](#)) with 100 walkers, 1000 iterations, and a burn-in length of 1000. The total scatter of data values (i) was assumed to follow a Gaussian distribution with standard deviation of σ_{tot} calculated as

$$\sigma_{\text{tot},i} = \sqrt{\sigma_{\text{stat},i}^2 + \sigma_{\text{spread}}^2(r_i)}. \quad (7)$$

For each iteration of the MCMC χ^2 was calculated as

$$\chi^2 = \sum_{i=1}^n \frac{(D_i - \mu(r_i))^2}{\sigma_{\text{tot},i}^2}, \quad (8)$$

where D_i are the individually measured values of the n data points (see Fig. 3). The mean model and spread values have $N + M$ free parameters. These parameters were varied via the MCMC method, giving the logarithm of the likelihood as the probability value for each iteration (see e.g. [Hogg et al. 2010](#)),

$$\log L = -\frac{1}{2} \chi^2 - \frac{1}{2} \sum_{i=1}^n \log(2\pi \sigma_{\text{tot},i}^2). \quad (9)$$

From this procedure we obtained a distribution of mean and spread values. We selected the best fit value for each parameter as the maximum of the distribution and estimated the uncertainty by giving the range containing 34 per cent of the obtained values on each side of the maximum. If the distribution was consistent with zero, we give the 68 per cent range as an upper limit.

The spread measurements performed with just one radial spread bin ($M = 1$) were used to compare the overall fractional spread dn , dT , dP , and dS among clusters (see e.g. Figs. 6, 7, 10, and Table C.1) and constrain the general ICM properties. For additional comparisons of larger and smaller physical radii, we measured the spread inside and outside of 100 kpc from the X-ray peak ($M = 2$, see e.g. dP_{cen} and dP_{out} , Sect. 4.2). From the spread analysis with five radial spread bins ($M = 5$), we obtained profiles of the intrinsic fractional standard deviation of thermodynamic properties dn/n , dT/T , dP/P , and dS/S (see Fig. F.1) in individual systems. The spread measurements are consistent with the results of a second Monte Carlo simulation-based technique, which was not based on Markov chains (similar to [Sanders et al. 2014](#)).

3.2. Surface brightness substructures

The emissivity of the ICM, and thus its surface brightness in X-rays, is proportional to the plasma density squared (for a review, see e.g. [Sarazin 1986](#)). From the data reduction pipeline we obtained merged count and exposure images of the clusters. To remove any structure due to inhomogeneous exposure, we divided the count image by the exposure image and obtained an image of the count rate. To identify small surface brightness fluctuations, we enhanced the contrast of those images by unsharp-masking, a method commonly used in image analysis. This method is implemented by subtracting two versions of an image, smoothed by two different Gaussian filters, from each other. We subtracted an image smoothed with a Gaussian function of $\sigma = 2$ pixel width from an image smoothed with a Gaussian function of $\sigma = 5$ pixel width (see Fig. E.1). The obtained unsharp-masked images enhance surface brightness features, complementing the analysis of substructure in thermodynamic properties and highlighting disturbed systems.

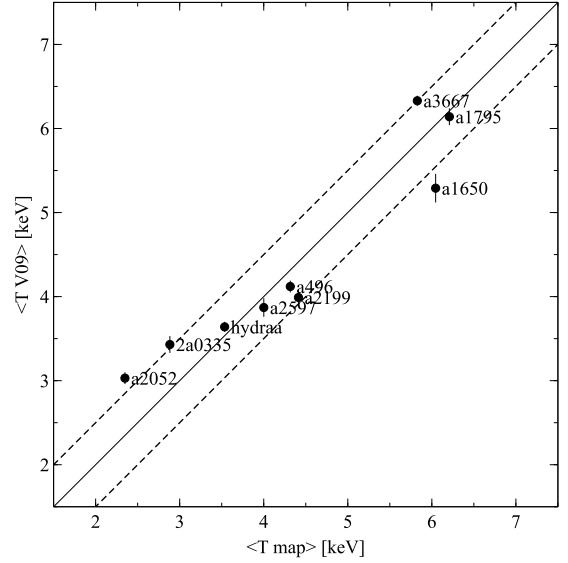


Fig. 4. Comparison of area- and error-weighted average 2D map temperatures $\langle T_{\text{map}} \rangle$ with overlapping low- z sample temperatures of V09 ([Vikhlinin et al. 2009a](#)) showing a scatter of about 0.5 keV around the one-to-one relation.

3.3. Average cluster temperatures

We calculated average cluster temperatures $\langle T_{\text{map}} \rangle$ as the area- and error-weighted mean value of all measurements. We computed the average of the bin temperature ($\langle T_{\text{prof}} \rangle$, see data points in Fig. 3), which is usually lower than $\langle T_{\text{map}} \rangle$ because $\langle T_{\text{prof}} \rangle$ is weighted more on emission than area. Hotter regions in the outskirts are generally larger with lower emission and the relatively colder, X-ray bright, central regions cover a smaller area.

We compared our approach for estimating overall cluster temperatures with previous studies like V09 using (using *Chandra*; [Vikhlinin et al. 2009a](#)) or HiFLUGS (using ROSAT; [Reiprich & Böhringer 2002](#)), as shown in Figs. 4 and 5. Figure 4 shows significant scatter of up to 0.5 keV between V09 and this study. This is expected since we use a different approach by averaging many independently fitted bins weighting by area and error bars rather than by counts. The averaging of many different bins results in small error bars on our average temperature. Figure 5 shows similar scatter when accounting for the larger error bars on the ROSAT measurements. We also use different extraction radii than our comparison studies, which influences the measured temperature.

To estimate the mass range of the cluster sample (see Table 1), we used the mass-temperature scaling relation from [Vikhlinin et al. \(2009a\)](#) with the $\langle T_{\text{map}} \rangle$ temperatures as input to calculate the overdensity radius r_{500} and the total mass M_{500} included by this radius. We accounted for uncertainties in the scaling by assuming a systematic temperature uncertainty of 0.5 keV (see scatter in Fig. 4). The average map temperature (area weighted) is comparable to the core-excised average temperature used for the scaling by [Vikhlinin et al. \(2009a\)](#).

3.4. Table description

The main results of the analysis of this study are summarised in separate tables for each cluster. We created 2D maps from the merged observations of every cluster and measured the

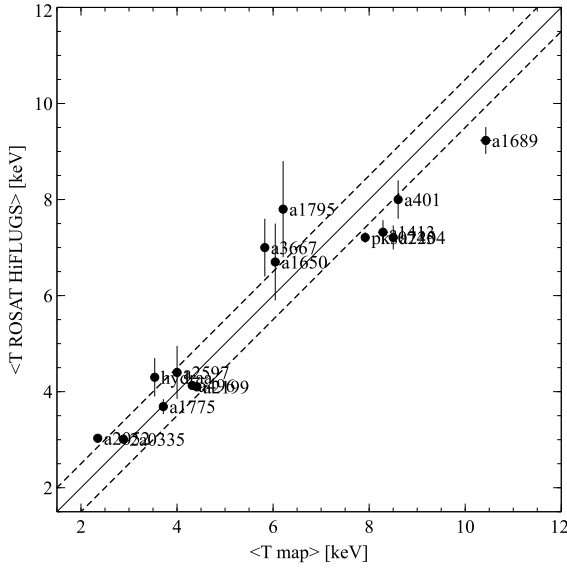


Fig. 5. Comparison of area- and error-weighted average 2D map temperatures ($\langle T \text{ map} \rangle$) with HiFLUGS temperatures (Reiprich & Böhringer 2002) from ROSAT observations for the clusters overlapping with our sample. The dashed lines show a one-to-one relation with a scatter of 0.5 keV.

asymmetries in thermodynamic parameters in circular concentric annuli around the centre.

3.4.1. Map tables

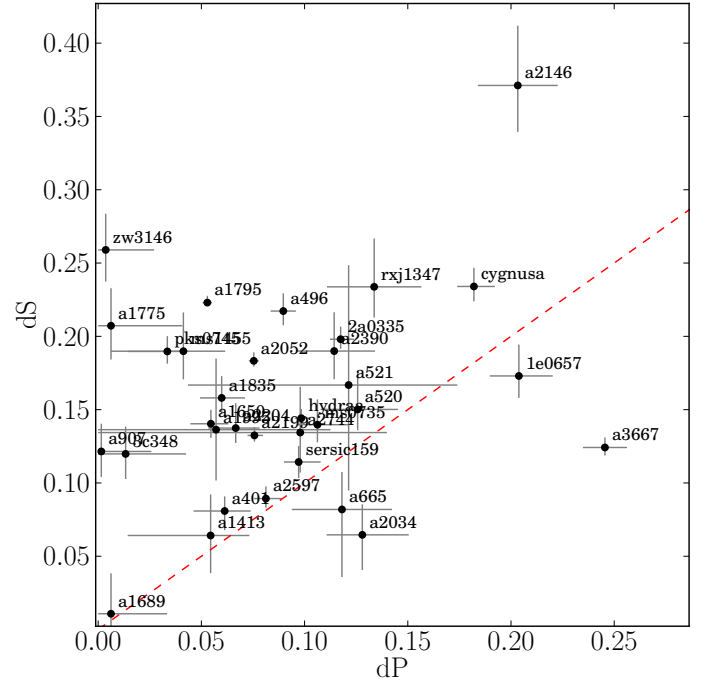
The primary data products of this analysis are 2D maps of the thermodynamic properties of the ICM based on the merged observations of ACIS-S and ACIS-I for every cluster in the sample (see Sect. 2.2).

Tables 2–34 contain the 2D map information (one table per cluster). Each table lists the properties for every pixel in the cluster maps (1 pix $\sim 0.98''$). The map tables contain the following: X (east-west direction) and Y (south-north direction) position (x , y , Cols. 1, 2) of the pixel; index of the independently-fitted, spatial-spectral bin it belongs to (binnum, Col. 3); photon counts (cts, Col. 4); the background counts (bgcts, Col. 5); effective exposure time (exp, Col. 6); temperature and its upper and lower limits (T , T_{up} , T_{lo} , Cols. 7–9); relative metallicity and limits (Z , Z_{up} , Z_{lo} , Cols. 10–12); fit normalisation and limits (norm, normup, normlo, Cols. 13–15); redshift (redshift, Col. 16); foreground column density n_{H} (N_{H} , Col. 17); distance from the centre in pixels, arc seconds, and kpc (cen_dist, rad_arcsec, rad_kpc, Cols. 18–20); angle with respect to the west direction (cen_angl, Col. 21); calculated projected pressure and symmetric uncertainty (P , P_{err} , Cols. 22, 23); projected entropy and uncertainty (S , S_{err} , Cols. 24, 25); and density and uncertainty (n , n_{err} , Cols. 26, 27). All uncertainties are on 1σ confidence level.

3.4.2. Asymmetry tables

The secondary data products are based on the 2D maps and contain the measured spread (i.e. asymmetry, deviation from radial symmetry) of the thermodynamic parameters; see $M = 5$ in Sect. 3.1).

Tables 35–67 provide the measured properties in the concentric annuli for one cluster each. They contain the average



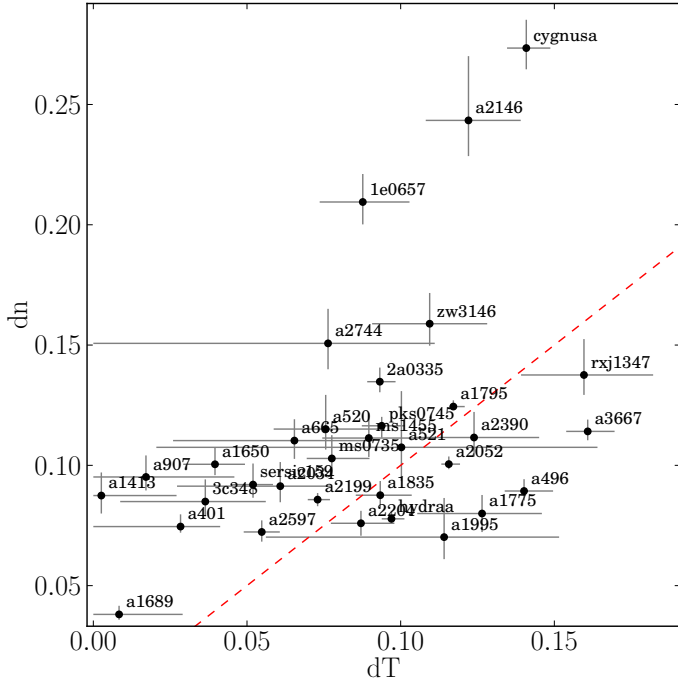


Fig. 7. Comparison of average temperature and projected density fluctuations for all clusters in the sample. The dashed line represents a one-to-one relation. Error bars are the statistical uncertainty from the MCMC measurements.

Table 68. Average perturbations.

$\langle dP \rangle^a$	$\langle dS \rangle^a$	$\langle dn \rangle^a$	$\langle dT \rangle^a$
0.09 ± 0.06	0.16 ± 0.07	0.11 ± 0.05	0.09 ± 0.04

Notes. ^(a) Average fractional perturbations in thermodynamic properties of the 33 sample clusters. Standard deviation as confidence range.

(fractional spread, dT). We measure a significant spread in dn for every cluster in the sample, but only obtain upper limits on the dT spread for some. There are some outliers that show very strong density fluctuations (e.g. A 2146, 1E 0657-56, and Cygnus A). Overall, most clusters are close to a one-to-one correlation with an average of 11 per cent fluctuations in density and 9 per cent in temperature (see Table 68).

4.2. Perturbations on different scales

We found evidence for larger pressure perturbations dP at larger scales. Figure 8 shows a clear separation of the distribution for central regions ≤ 100 kpc (cen) from the centre and regions beyond (out). To compare the distribution of spread values on different scales, we used the asymmetry measurements from Sect. 3.1, where the cluster profile is divided at ~ 100 kpc. The division at 100 kpc was chosen, after visual inspection, as a robust separation radius between central substructure and outer more homogeneous regions. We did not choose the regions relative to r_{500} to ensure we are testing the same physical scale of the ICM fluctuations.

We used a bootstrapping re-sampling technique, calculating the mean value for 1000 permutations with repetition, to estimate the mean of the distributions. The contours are at 15, 50, and 85 percent of the maximum of the obtained distribution of mean values. In addition, Fig. 8 contains the output

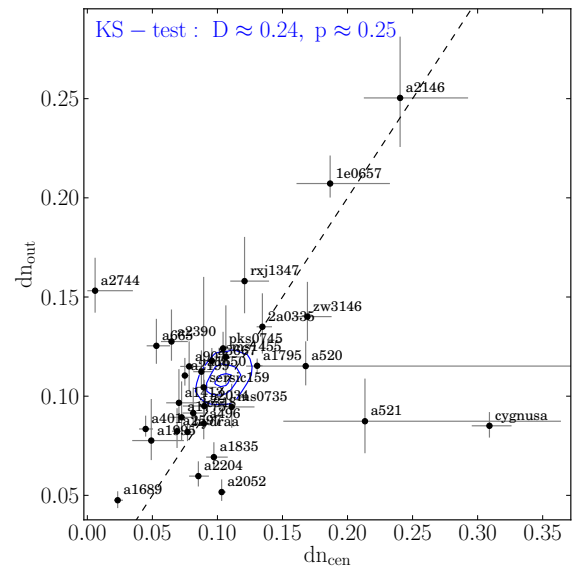
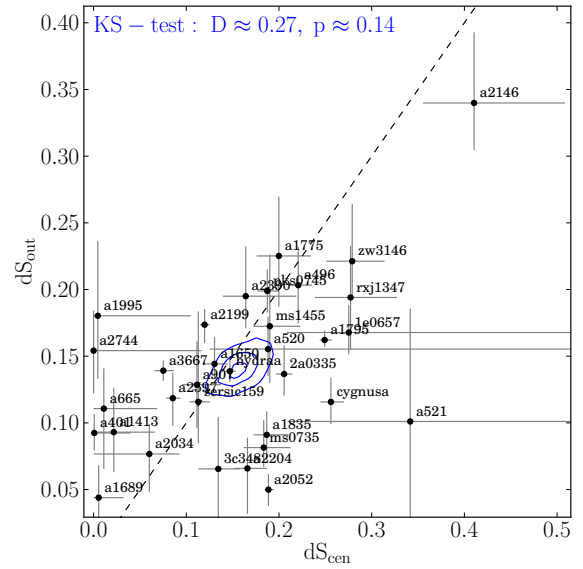
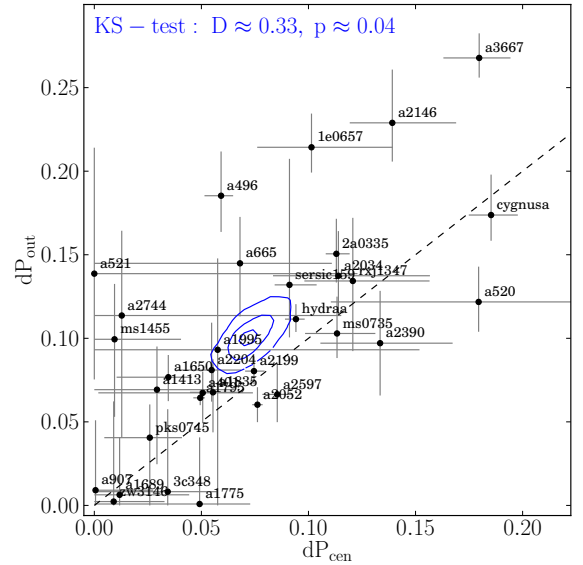


Fig. 8. Comparison of pressure (top), entropy (middle), and density perturbations (bottom) in the central ≤ 100 kpc and outer ≥ 100 kpc regions. Confidence regions of the mean value as contours (85, 50, and 15 per cent of peak value). KS test results on top. One-to-one correlation as dashed line.

the fit uncertainties are larger because of overlapping chip gaps of many observations, which could bias our results (see faint spurious linear structures in Fig. D.1).

Abell 496 is a relaxed cluster with relatively high metallicity around the cool core and non-uniform temperature distribution on large scales (Tamura et al. 2001; Tanaka et al. 2006; Ghizzardi et al. 2014). By comparing dedicated simulations of the cluster to deep *Chandra* observations, Roediger et al. (2012) concluded that the cluster was most likely perturbed by a merging subcluster 0.6–0.8 Gyr ago.

The spiral surface brightness excess structure and the northern cold front is clearly visible in our new images of temperature and unsharp-masked count images (see Figs. D.1, E.1). The radial profiles and asymmetry measurements show relatively large spread in entropy (see Fig. F.1). Figures 6 and 7 show that the cluster has a large average temperature spread (as a result of the large scale asymmetry caused by the sloshing of colder gas from the centre) and thus also larger spread in entropy. A 496 has a flat pressure profile similar to the strongest merging systems in the sample. The average metallicity is the highest we measured.

PKS0745-191 is a relaxed cluster at large scales out to the virial radius (George et al. 2009). Sanders et al. (2014) found AGN feedback and sloshing structures in deep *Chandra* observations.

The AGN feedback features are most prominent in the unsharp-masked image (Fig. E.1) and indications of weak asymmetry in temperature on large scales can be seen in Fig. D.1. The radial profiles of the cluster follow the expected trend for relaxed systems, but show remarkably low intrinsic scatter in pressure and relatively high scatter in entropy (see Fig. F.1). The scatter measurements of Sanders et al. (2014) are consistent with our method for dn , dT , dP , and dS . This is the only cluster in the sample where n_H was set as a free parameter in the spectral fits because the foreground column density of this system is known to vary significantly.

6. Discussion

The perturbation measurements for this cluster sample constrain the average Mach number of the systems. The sample covers a wide range of dynamic ICM states, providing insight into the influence of different perturbation events.

6.1. Caveats of perturbation measurements

It has been shown by Sanders et al. (2014) that in the PKS0745-191 cluster projection effects in the measured parameters caused the calculated projected spread to be only about half of the real spread in the ICM. Therefore, we expect projection effects to strongly affect the absolute values of our spread parameters. Since the effect seems to be similar for all parameters in the PKS0745-191 system, the comparison of ratios between different spreads should not be affected. All asymmetry measurements are based on circular extraction regions, which means ellipticity of the cluster emission, as in PKS0745-191, adds to the spread values. Thus, strong ellipticity could also influence the measured ratios between perturbations. Sanders et al. (2014) showed for PKS0745-191 that different bin sizes within a certain range lead to consistent results in the spread analysis. However, if the bins are too large, as for some more distant clusters in our sample, we generally obtain larger absolute spread values (e.g. zw3146

in Fig. 6). Overall the comparison of spread measurements on maps with a S/N of 25 and 50 were in good agreement.

In real clusters there are many factors influencing perturbation measurements. The clusters that lie outside the relations expected from simulations seem to be dominated by processes that have not been included in the simulations (like mergers, AGN feedback bubbles, shocks, or uplifted cold gas). Also projection effects in our measurements and the overall geometry of a system could cause deviations. We emphasise the parameters dS and dP are not independent, since they are derived from the independent fit parameters T and η (see Sect. 2.2). Uncertainties in the spectral fits are larger at higher temperatures. The size of the error bars of individual measurements limit the sensitivity for finding additional spread in the MCMC calculations (see Sect. 3.1). In the case of Abell 1689, the absolute spread measurements are very low and we only obtain upper limits for this system, which is caused by very low fluctuations and high temperatures, lowering the sensitivity for detecting additional spread.

With the caveats described above, our measurements allow for a rough estimate of the average Mach number and thus turbulence trends in the ICM for a large sample of massive clusters of galaxies. Future simulations help to better quantify the influence of the above described caveats on the Mach number estimates.

6.2. Relating perturbations to turbulence

Recent high-resolution 3D hydrodynamic simulations by Gaspari et al. (2014) show that entropy and pressure drive the main perturbations in the ICM, depending on the Mach number in the medium. In the low Mach number case ($\text{Mach}_{3D} < 0.5$) perturbations are mainly isobaric, implying

dP/P is negligible, $dS/S \sim \text{Mach}_{1D}$, and $dn/n \sim |dT/T|$.

For large Mach numbers ($\text{Mach}_{3D} > 0.5$), perturbations shift to the adiabatic regime because turbulence becomes more violent, overcoming the cluster stratification, implying

dS/S becomes negligible, $dP/P \sim \text{Mach}_{1D}$, and $dn/n \sim 1/(\gamma - 1) dT/T \sim 1.5 dT/T$.

The measurements of the average perturbations in the sample suggest a mixture of the two states (see Figs. 6 and 7). We observed that entropy perturbations are slightly dominating pressure fluctuations (Fig. 6) and density fluctuations are comparable to temperature fluctuations with a possible tendency of slightly dominating dn (Fig. 7). Enhanced temperature asymmetry can be caused by displaced cold gas from the central region due to strong feedback like e.g. in Cygnus A or strong cold fronts, as observed in Abell 3667. Additional conduction in the ICM can weaken temperature perturbations (Gaspari et al. 2014).

Assuming entropy perturbations dominate in the sample, it follows that $dS/S \sim \text{Mach}_{1D}$. The dS/S value is related to the normalisation of the power spectrum, which is related to the peak of the power spectrum that occurs at large physical radii (low wavenumber k), typically ≥ 100 kpc or $\geq 0.1 r_{500}$. As an approximation, we used the overall average of perturbations ($M = 1$, see Sect. 3.1) as a turbulence indicator since the assumption is that dS dominates does not hold in the outer regions ≥ 100 kpc of the clusters (see Sect. 4.2). The measurements on average suggest $\text{Mach}_{1D} \approx 0.16 \pm 0.07$ (see Fig. 10).

Hydrodynamical simulations of galaxy clusters usually find the ratio between turbulence energy E_{turb} and the thermal

energy E_{therm} to be $E_{\text{turb}} \approx 3\text{--}30\% E_{\text{therm}}$, from relaxed to unrelaxed clusters (Norman & Bryan 1999; Vazza et al. 2009; Lau et al. 2009; Vazza et al. 2011, 2012; Gaspari et al. 2012b; Miniati 2014; Schmidt et al. 2014). Since

$$E_{\text{turb}} = 0.5 \gamma (\gamma - 1) \text{Mach}_{3\text{D}}^2 E_{\text{therm}} \approx 0.56 \text{Mach}_{3\text{D}}^2 E_{\text{therm}}, \quad (10)$$

where the adiabatic index $\gamma = C_P/C_V = 5/3$ (C_P, C_V heat capacity of the medium at constant pressure and volume, respectively), it follows that $\text{Mach}_{3\text{D}} \approx 0.23\text{--}0.73$ and thereby,

$$\text{Mach}_{1\text{D}} = \text{Mach}_{3\text{D}}/\sqrt{3} \approx 0.13\text{--}0.42, \quad (11)$$

which is consistent with the measured average of $\text{Mach}_{1\text{D}} \approx 0.16 \pm 0.07$. This would suggest that turbulence energy in this sample of clusters is on average about four per cent of the thermal energy in the systems. Figure 10 indicates a weak anti-correlation with average cluster temperature. In the best-fit linear regression $\text{Mach}_{1\text{D}} \approx -(0.01 \pm 0.01) \langle T_{\text{prof}} \rangle / \text{keV} + (0.20 \pm 0.05)$, the slope is consistent with zero within the errors. The significance of the slope was estimated using the re-sampling technique of Sect. 4.3 by investigating the distribution of fit functions in 1000 fits to random subsamples of half the size of the original. The absolute values used as Mach number indicator are subject to some uncertainty, such as projection and feedback effects that have not been taken into account in the comparison simulations (see Sect. 6.1).

6.3. Difference between core and outskirts

If the enhanced pressure perturbations in the outer regions of the clusters in this sample can be confirmed, this could be interpreted as a change in the thermodynamic state of the ICM from the centre to the outer regions. With increasing pressure perturbations dP we expect more turbulent, pressure-wave driven motions in the ICM.

This fits the expectation of less relaxed outer regions in clusters where the ICM is not yet virialised and still being accreted into the cluster potential (e.g. Lau et al. 2009). The change of the dP/dS ratio could also be due to the dependence of the ratio on the probed scales (e.g. Gaspari & Churazov 2013; Gaspari et al. 2014). In annuli at larger radii we probe larger scales of ICM fluctuations. A change in dP/dS with scale would also show a radial dependence in the sample.

6.4. ICM metallicity

The metallicity of the ICM and its local distribution are of great interest when studying the processes that are enriching the ICM with heavier nuclei. These metals are thought to be mainly produced by supernova explosions in the galaxies (mainly in the brightest clusters galaxy, BCG) within the clusters and then transported into the ICM (see e.g. Böhringer & Werner 2010; de Plaa et al. 2007).

The observed anti-correlation between average cluster temperature and metallicity (Fig. 9) could have many different causes. Sanders et al. (2004) found a similar relation between metallicity and temperature in the Perseus cluster. After testing for various systematic effects they found the correlation to be real, but no definite explanation for the effect has been found so far. Sloshing structures of colder gas have been found to coincide with higher metallicity (see e.g. Roediger et al. 2011), which could partially explain an anti-correlation.

The temperatures of the clusters in our sample are correlated to their redshift and the metallicity anti-correlates with redshift as well as temperature. Balestra et al. (2007) probed a sample of clusters in the redshift range $0.3 < z < 1.3$ and found significant evolution in metallicity between their higher and lower redshift clusters by more than a factor of two. This trend was confirmed by Maughan et al. (2008). Both studies also found a correlation between cluster temperature and metallicity. However, e.g. Baldi et al. (2012) found no significant evolution of abundance with redshift. It is not clear whether to expect any evolution within the narrow redshift range ($0.025 \leq z \leq 0.45$) we probed. This corresponds to a time span of $\Delta t \approx 4$ Gyr in the standard cosmology assumed in this study.

In individual clusters there is a general trend of lower metallicity at larger radii (see also De Grandi & Molendi 2001; Sanders et al. 2004; Leccardi & Molendi 2008), which means the average metallicity is lower when we cover larger radial ranges for clusters at higher redshift. The metallicity drops from the centres ($Z_{\text{solar}} \approx 0.4\text{--}0.8$) with typically lower temperature gas out to ~ 300 kpc, where the profile flattens around a metallicity fraction of 0.2 solar. Uniform metallicity distribution at larger radii has been observed in great detail in the Perseus cluster (Werner et al. 2013).

The colder gas generally resides in the cluster centres, often in the vicinity of large cD galaxies that might cause enhanced enrichment. More massive (higher temperature) systems will have also undergone more mergers and generally have stronger AGN feedback, which contributes to the dilution of metals in the X-ray halo (e.g. Gaspari et al. 2011) and affects the average area- and error-weighted metallicity calculated in this study. Also, the multiphasedness of the hot ICM along the line of sight could influence the correlation as we typically probe larger volumes for higher temperatures. Multiphase gas has been found to bias the ICM metallicity measurements from X-ray spectra in some clusters (e.g. Panagoulia et al. 2013). Unresolved 2D structure of the ICM could bias the measured metallicity to higher values for systems with intermediate temperatures (see Rasia et al. 2008; Simionescu et al. 2009; Gastaldello et al. 2010). This study reduced multiphase effects by resolving the spatial structure and measuring the average metallicity of many spatial-spectral bins.

Another factor of influence could be that star formation efficiency decreases with cluster mass and temperature (e.g. Böhringer & Werner 2010). There have been many studies in the infrared wavelength (e.g. Popesso et al. 2012, 2015) that show quenching of star formation in massive DM halos of galaxy clusters and groups. Our sample predominantly consists of relatively massive systems (see Table 1) at low to intermediate redshifts and in different stages of evolution. All metallicity measurements are based on a fixed solar abundance model (Anders & Grevesse 1989).

7. Summary and conclusions

We presented a very large sample of detailed cluster maps with application to understand the thermodynamic processes in clusters of galaxies. The deep observations of the individual clusters helped to identify structures in the ICM caused by mergers or AGN feedback. By comparing perturbations in the sample with recent high-resolution simulations of perturbations in the ICM, we constrained the average 1D Mach number regime in the sample to $\text{Mach}_{1\text{D}} \approx 0.16 \pm 0.07$ with some caveats (see Sect. 6). In comparison with simulations, this result would suggest $E_{\text{turb}} \approx 0.04 E_{\text{therm}}$ (see Sect. 6.2). By comparing perturbations in the central regions ($\lesssim 100$ kpc) and in the outer regions

(≥ 100 kpc), we found an indication for a change in the thermodynamic state from mainly isobaric to a more adiabatic regime.

In addition, the sample shows a tight correlation between the average cluster metallicity, average temperature, and redshift. The best-fit linear correlation between metallicity and redshift is $Z/Z_{\odot} = -(0.6 \pm 0.2) z + (0.36 \pm 0.04)$ and between metallicity and temperature the best fit is $Z/Z_{\odot} = -(1.0 \pm 0.7) T/100 \text{ keV} + (0.34 \pm 0.06)$. The average metallicity of the sample is $Z \approx 0.3 \pm 0.1 Z_{\odot}$.

Future X-ray missions like Astro-H (Kitayama et al. 2014) and Athena (Nandra et al. 2013) will help to further investigate turbulent velocities and chemical enrichment in the ICM. The eROSITA observatory (Merloni et al. 2012) will detect a large X-ray cluster sample for cosmological studies and our detailed cluster mapping can be used to make predictions on the scatter in scaling relations due to unresolved structures in temperature. To encourage further analysis based on this unique sample of cluster observations, all maps and asymmetry measurements used in this study are made available publicly in electronic form.

Acknowledgements. We thank the anonymous referee for constructive comments that helped to improve the clarity of the paper. We thank J. Buchner for helpful discussions. This research has made use of data obtained from the *Chandra* Data Archive and the *Chandra* Source Catalog, and software provided by the *Chandra* X-ray Center (CXC) in the application packages CIAO, ChIPS, and Sherpa. This research has made use of NASA's Astrophysics Data System. This research has made use of the Vizier catalogue access tool, CDS, Strasbourg, France. This research has made use of SAOImage DS9, developed by the Smithsonian Astrophysical Observatory. This research has made use of data and software provided by the High Energy Astrophysics Science Archive Research Center (HEASARC), which is a service of the Astrophysics Science Division at NASA/GSFC and the High Energy Astrophysics Division of the Smithsonian Astrophysical Observatory. This research has made use of the SIMBAD database, operated at CDS, Strasbourg, France. This research has made use of the tools Veusz, the matplotlib library for Python, and TOPCAT. M.G. is supported by the National Aeronautics and Space Administration through Einstein Postdoctoral Fellowship Award Number PF-160137 issued by the *Chandra* X-ray Observatory Center, which is operated by the Smithsonian Astrophysical Observatory for and on behalf of the National Aeronautics Space Administration under contract NAS8-03060.

References

- Allen, S. W., Schmidt, R. W., & Fabian, A. C. 2002, *MNRAS*, **334**, L11
- Allen, S. W., Schmidt, R. W., Ebeling, H., Fabian, A. C., & van Speybroeck, L. 2004, *MNRAS*, **353**, 457
- Allen, S. W., Rapetti, D. A., Schmidt, R. W., et al. 2008, *MNRAS*, **383**, 879
- Anders, E., & Grevesse, N. 1989, *Geochim. Cosmochim. Acta*, **53**, 197
- Arnaud, K. A. 1996, in *Cosmic Abundances*, eds. S. S. Holt, & G. Sonneborn, *ASP Conf. Ser.*, **99**, 409
- Baldi, A., Ettori, S., Molendi, S., Balestra, I., et al. 2012, *A&A*, **537**, A142
- Balestra, I., Tozzi, P., Ettori, S., et al. 2007, *A&A*, **462**, 429
- Blanton, E. L., Sarazin, C. L., McNamara, B. R., & Wise, M. W. 2001, *ApJ*, **558**, L15
- Blanton, E. L., Sarazin, C. L., & McNamara, B. R. 2003, *ApJ*, **585**, 227
- Blanton, E. L., Randall, S. W., Clarke, T. E., et al. 2011, *ApJ*, **737**, 99
- Böhringer, H., & Werner, N. 2010, *A&ARv*, **18**, 127
- Böhringer, H., Voges, W., Huchra, J. P., et al. 2000, *ApJS*, **129**, 435
- Böhringer, H., Schuecker, P., Guzzo, L., et al. 2004, *A&A*, **425**, 367
- Bradač, M., Clowe, D., Gonzalez, A. H., et al. 2006, *ApJ*, **652**, 937
- Broadhurst, T. J., Taylor, A. N., & Peacock, J. A. 1995, *ApJ*, **438**, 49
- Canning, R. E. A., Russell, H. R., Hatch, N. A., et al. 2012, *MNRAS*, **420**, 2956
- Cash, W. 1979, *ApJ*, **228**, 939
- Clowe, D., Gonzalez, A., & Markevitch, M. 2004, *ApJ*, **604**, 596
- Clowe, D., Bradač, M., Gonzalez, A. H., et al. 2006, *ApJ*, **648**, L109
- De Grandi, S., & Molendi, S. 2001, *ApJ*, **551**, 153
- de Plaa, J., Werner, N., Bleeker, J. A. M., et al. 2007, *A&A*, **465**, 345
- Dennis, T. J., & Chandran, B. D. G. 2005, *ApJ*, **622**, 205
- Dolag, K., Schindler, S., Govoni, F., & Feretti, L. 2001, *A&A*, **378**, 777
- Dolag, K., Vazza, F., Brunetti, G., & Tormen, G. 2005, *MNRAS*, **364**, 753
- Ebeling, H., Mullis, C. R., & Tully, R. B. 2002, *ApJ*, **580**, 774
- Ehler, S., McDonald, M., David, L. P., Miller, E. D., & Bautz, M. W. 2015, *ApJ*, **799**, 174
- Ettori, S., Fabian, A. C., Allen, S. W., & Johnstone, R. M. 2002, *MNRAS*, **331**, 635
- Fabian, A. C. 1994, *ARA&A*, **32**, 277
- Fabian, A. C., Sanders, J. S., Ettori, S., et al. 2000, *MNRAS*, **318**, L65
- Fabian, A. C., Sanders, J. S., Ettori, S., et al. 2001, *MNRAS*, **321**, L33
- Fabian, A. C., Sanders, J. S., Taylor, G. B., et al. 2006, *MNRAS*, **366**, 417
- Foreman-Mackey, D., Hogg, D. W., Lang, D., & Goodman, J. 2013, *PASP*, **125**, 306
- Forman, W., Jones, C., Churazov, E., et al. 2007, *ApJ*, **665**, 1057
- Foster, A. R., Ji, L., Smith, R. K., & Brickhouse, N. S. 2012, *ApJ*, **756**, 128
- Fruscione, A., McDowell, J. C., Allen, G. E., et al. 2006, in *SPIE Conf. Ser.*, **6270**, 1
- Garmire, G. P., Bautz, M. W., Ford, P. G., Nousek, J. A., & Ricker, Jr., G. R. 2003, in *X-Ray and Gamma-Ray Telescopes and Instruments for Astronomy*, eds. J. E. Truemper, & H. D. Tananbaum, *SPIE Conf. Ser.*, **4851**, 28
- Gaspari, M., & Churazov, E. 2013, *A&A*, **559**, A78
- Gaspari, M., Melioli, C., Brighenti, F., & D'Ercole, A. 2011, *MNRAS*, **411**, 349
- Gaspari, M., Brighenti, F., & Temi, P. 2012a, *MNRAS*, **424**, 190
- Gaspari, M., Ruszkowski, M., & Sharma, P. 2012b, *ApJ*, **746**, 94
- Gaspari, M., Churazov, E., Nagai, D., & Lau, E. T., & Zhuravleva, I. 2014, *A&A*, **569**, A67
- Gastaldello, F., Ettori, S., Balestra, I., et al. 2010, *A&A*, **522**, A34
- George, M. R., Fabian, A. C., Sanders, J. S., Young, A. J., & Russell, H. R. 2009, *MNRAS*, **395**, 657
- Ghizzardi, S., De Grandi, S., & Molendi, S. 2014, *A&A*, **570**, A117
- Govoni, F., Markevitch, M., Vikhlinin, A., et al. 2004, *ApJ*, **605**, 695
- Graessle, D. E., Evans, I. N., Glotfelty, K., et al. 2007, *Chandra News*, **14**, 33
- Hogg, D. W., Bovy, J., & Lang, D. 2010, ArXiv e-prints [[arXiv:1008.4686](https://arxiv.org/abs/1008.4686)]
- Johnstone, R. M., Allen, S. W., Fabian, A. C., & Sanders, J. S. 2002, *MNRAS*, **336**, 299
- Kaiser, N., Squires, G., & Broadhurst, T. 1995, *ApJ*, **449**, 460
- Kalberla, P. M. W., Burton, W. B., Hartmann, D., et al. 2005, *A&A*, **440**, 775
- Kitayama, T., Bautz, M., Markevitch, M., et al. 2014, ArXiv e-prints [[arXiv:1412.1176](https://arxiv.org/abs/1412.1176)]
- Lau, E. T., Kravtsov, A. V., & Nagai, D. 2009, *ApJ*, **705**, 1129
- Leccardi, A., & Molendi, S. 2008, *A&A*, **487**, 461
- Machado, R. E. G., & Lima Neto, G. B. 2015, *MNRAS*, **447**, 2915
- Mahdavi, A., Hoekstra, H., Babul, A., et al. 2013, *ApJ*, **767**, 116
- Markevitch, M., Vikhlinin, A., Forman, W. R., & Sarazin, C. L. 1999, *ApJ*, **527**, 545
- Markevitch, M., Ponman, T. J., Nulsen, P. E. J., et al. 2000, *ApJ*, **541**, 542
- Markevitch, M., Vikhlinin, A., & Mazzotta, P. 2001, *ApJ*, **562**, L153
- Markevitch, M., Gonzalez, A. H., David, L., et al. 2002, *ApJ*, **567**, L27
- Markevitch, M., Bautz, M. W., Biller, B., et al. 2003, *ApJ*, **583**, 70
- Markevitch, M., Gonzalez, A. H., Clowe, D., et al. 2004, *ApJ*, **606**, 819
- Maughan, B. J., Jones, C., Forman, W., & Van Speybroeck, L. 2008, *ApJS*, **174**, 117
- McDonald, M., Veilleux, S., Rupke, D. S. N., Mushotzky, R., & Reynolds, C. 2011, *ApJ*, **734**, 95
- McNamara, B. R., Wise, M., Nulsen, P. E. J., et al. 2000, *ApJ*, **534**, L135
- Merloni, A., Predehl, P., Becker, W., et al. 2012, ArXiv e-prints [[arXiv:1209.3114](https://arxiv.org/abs/1209.3114)]
- Miniati, F. 2014, *ApJ*, **782**, 21
- Nandra, K., Barret, D., Barcons, X., et al. 2013, ArXiv e-prints [[arXiv:1306.2307](https://arxiv.org/abs/1306.2307)]
- Nelson, K., Lau, E. T., & Nagai, D. 2014, *ApJ*, **792**, 25
- Norman, M. L., & Bryan, G. L. 1999, in *Lecture Notes in Physics, The Radio Galaxy Messier 87*, eds. H.-J. Röser, & K. Meisenheimer (Berlin Springer Verlag), 530, 106
- Nulsen, P. E. J., David, L. P., McNamara, B. R., et al. 2002, *ApJ*, **568**, 163
- Nulsen, P. E. J., McNamara, B. R., Wise, M. W., & David, L. P. 2005, *ApJ*, **628**, 629
- Nulsen, P. E. J., Li, Z., Forman, W. R., et al. 2013, *ApJ*, **775**, 117
- Oegerle, W. R., & Hill, J. M. 1994, *AJ*, **107**, 857
- Panagoulia, E. K., Fabian, A. C., & Sanders, J. S. 2013, *MNRAS*, **433**, 3290
- Pinto, C., Sanders, J. S., Werner, N., et al. 2015, *A&A*, **575**, A38
- Popesso, P., Biviano, A., Rodighiero, G., et al. 2012, *A&A*, **537**, A58
- Popesso, P., Biviano, A., Finoguenov, A., et al. 2015, *A&A*, **574**, A105
- Randall, S. W., Markevitch, M., Clowe, D., Gonzalez, A. H., & Bradač, M. 2008, *ApJ*, **679**, 1173
- Rasia, E., Mazzotta, P., Bourdin, H., et al. 2008, *ApJ*, **674**, 728
- Reiprich, T. H., & Böhringer, H. 2002, *ApJ*, **567**, 716
- Rines, K., Geller, M. J., Diaferio, A., & Kurtz, M. J. 2013, *ApJ*, **767**, 15
- Roediger, E., Brügger, M., Simionescu, A., et al. 2011, *MNRAS*, **413**, 2057
- Roediger, E., Lovisari, L., Dupke, R., et al. 2012, *MNRAS*, **420**, 3632
- Russell, H. R., Sanders, J. S., Fabian, A. C., et al. 2010, *MNRAS*, **406**, 1721
- Russell, H. R., van Weeren, R. J., Edge, A. C., et al. 2011, *MNRAS*, **417**, L1
- Russell, H. R., McNamara, B. R., Sanders, J. S., et al. 2012, *MNRAS*, **423**, 236

- Ruszkowski, M., & Oh, S. P. 2010, *ApJ*, 713, 1332
- Sanders, J. S. 2006, *MNRAS*, 371, 829
- Sanders, J. S., & Fabian, A. C. 2006, *MNRAS*, 371, L65
- Sanders, J. S., & Fabian, A. C. 2013, *MNRAS*, 429, 2727
- Sanders, J. S., Fabian, A. C., Allen, S. W., & Schmidt, R. W. 2004, *MNRAS*, 349, 952
- Sanders, J. S., Fabian, A. C., & Taylor, G. B. 2005, *MNRAS*, 356, 1022
- Sanders, J. S., Fabian, A. C., & Smith, R. K. 2011, *MNRAS*, 410, 1797
- Sanders, J. S., Fabian, A. C., Hlavacek-Larrondo, J., et al. 2014, *MNRAS*, 444, 1497
- Sarazin, C. L. 1986, *Rev. Mod. Phys.*, 58, 1
- Schmidt, W., Almgren, A. S., Braun, H., et al. 2014, *MNRAS*, 440, 3051
- Schuecker, P., Finoguenov, A., Miniati, F., Böhringer, H., & Briel, U. G. 2004, *A&A*, 426, 387
- Simionescu, A., Werner, N., Böhringer, H., et al. 2009, *A&A*, 493, 409
- Smith, D. A., Wilson, A. S., Arnaud, K. A., Terashima, Y., & Young, A. J. 2002, *ApJ*, 565, 195
- Springel, V., White, S. D. M., Jenkins, A., et al. 2005, *Nature*, 435, 629
- Tamura, T., Bleeker, J. A. M., Kaastra, J. S., Ferrigno, C., & Molendi, S. 2001, *A&A*, 379, 107
- Tanaka, T., Kunieda, H., Hudaverdi, M., Furuzawa, A., & Tawara, Y. 2006, *PASJ*, 58, 703
- Truemper, J. 1982, *Adv. Space Res.*, 2, 241
- Vazza, F., Brunetti, G., Kritsuk, A., Wagner, R., Gheller, C., & Norman, M. 2009, *A&A*, 504, 33
- Vazza, F., Brunetti, G., Gheller, C., Brunino, R., & Brüggén, M. 2011, *A&A*, 529, A17
- Vazza, F., Roediger, E., & Brüggén, M. 2012, *A&A*, 544, A103
- Vikhlinin, A., Burenin, R. A., Ebeling, H., et al. 2009a, *ApJ*, 692, 1033
- Vikhlinin, A., Kravtsov, A. V., Burenin, R. A., et al. 2009b, *ApJ*, 692, 1060
- Voit, G. M. 2005, *Rev. Mod. Phys.*, 77, 207
- Walker, S. A., Fabian, A. C., & Kosec, P. 2014, *MNRAS*, 445, 3444
- Werner, N., Urban, O., Simionescu, A., & Allen, S. W. 2013, *Nature*, 502, 656
- Zhang, Y.-Y., Finoguenov, A., Böhringer, H., et al. 2008, *A&A*, 482, 451
- Zhang, Y.-Y., Andernach, H., Caretta, C. A., et al. 2011, *A&A*, 526, A105
- Zhuravleva, I., Churazov, E., Schekochihin, A. A., et al. 2014, *Nature*, 515, 85

Appendix A: Cluster sample

Table A.1. *Chandra* cluster sample (CIZA clusters).

Cluster ^a	Exp. ^b [ks]	RA (J2000) [deg]	DEC (J2000) [deg]	Flux ^c [10 ⁻¹⁵ W/m ²]	<i>z</i>	Obj. ID (CIZA)	<i>L_X</i> ^d [10 ³⁷ W]
CYGNUS A	232	299.877	40.741	52.82	0.0561	J1959.5+4044	7.08
PKS 0745-191	174	116.883	-19.290	45.73	0.1028	J0747.5-1917	20.36

Notes. ^(a) Most commonly used name of cluster or central object. ^(b) Combined ACIS-S/I exposure after excluding times of high background. ^(c) ROSAT 0.1–2.4 keV X-ray flux in 10⁻¹⁵ W/m². ^(d) ROSAT 0.1–2.4 keV X-ray luminosity in 10³⁷ W (CIZA column: LX).

Table A.2. *Chandra* cluster sample (NORAS clusters).

Cluster ^a	Exp. ^b [ks]	RA (J2000) [deg]	Dec (J2000) [deg]	Flux ^c [10 ⁻¹⁵ W/m ²]	<i>z</i>	Obj. ID (NORAS)	<i>L_X</i> ^d [10 ³⁷ W]
A 2052	651	229.182	7.013	47.94	0.0353	RXC J1516.7+0701	2.58
A 1775	99	205.448	26.352	12.58	0.0724	RXC J1341.8+2622	2.83
A 2199	156	247.188	39.553	97.92	0.0299	RXC J1628.6+3932	3.77
2A 0335+096	102	54.665	10.007	80.91	0.0347	RXC J0338.6+0958	4.21
3C348 (HERCULES A)	112	252.778	4.985	5.39	0.154	RXC J1651.1+0459	5.49
A 2034	255	227.532	33.515	11.94	0.113	RXC J1510.1+3330	6.49
MS0735.6+7421	520	115.421	74.266	4.06	0.2149	RXC J0741.7+7414	7.94
A 2146	418	239.006	66.352	3.99	0.2339	RXC J1556.1+6621	9.31
A 1795	958	207.221	26.596	59.29	0.0622	RXC J1348.8+2635	9.93
A 1413	136	178.769	23.369	12.61	0.1427	RXC J1155.3+2324	10.91
A 401	163	44.727	13.579	50.29	0.0739	RXC J0258.9+1334	11.76
A 1995	100	223.168	58.049	3.18	0.3179	RXC J1452.9+5802	13.42
MS 1455.0+2232	108	224.253	22.33	4.89	0.2579	RXC J1457.2+2220	13.73
A 520	527	73.546	2.977	8.33	0.203	RXC J0454.1+0255	14.52
A 665	140	127.637	65.89	11.18	0.1818	RXC J0830.9+6551	15.69
A 2204	97	248.186	5.557	24.11	0.1514	RXC J1632.7+0534	23.43
A 2390	110	328.403	17.683	11.01	0.2329	RXC J2153.5+1741	25.15
ZW 3146	84	155.906	4.167	8.77	0.285	RXC J1023.6+0411	29.91
A 1835	223	210.271	2.895	12.12	0.2528	RXC J1401.0+0252	32.56

Notes. ^(a) Most commonly used name of cluster or central object. ^(b) Combined ACIS-S/I exposure after excluding times of high background. ^(c) ROSAT 0.1–2.4 keV X-ray flux in 10⁻¹⁵ W/m². ^(d) ROSAT 0.1–2.4 keV X-ray luminosity in 10³⁷ W (NORAS column: LX).

Table A.3. *Chandra* cluster sample (REFLEX clusters).

Cluster ^a	Exp. ^b [ks]	RA (J2000) [deg]	Dec (J2000) [deg]	Flux ^c [10 ⁻¹⁵ W/m ²]	<i>z</i>	Obj. ID (REFLEX)	<i>L_X</i> ^d [10 ³⁷ W]
SERSIC 159-03	106	348.515	-42.713	23.412	0.0564	J2313.9-4244	3.74
A 496	88	68.403	-13.25	72.075	0.0326	J0433.6-1315	3.89
HYDRA A	224	139.527	-12.092	39.461	0.0539	J0918.1-1205	5.61
A 1650	229	194.664	-1.781	20.909	0.0845	J1258.6-0145	6.99
A 2597	146	351.337	-12.136	20.558	0.0852	J2325.3-1207	7.22
A 3667	528	303.211	-56.855	70.892	0.0556	J2012.5-5649	10.02
A 907	103	149.528	-11.086	7.833	0.1669	J0958.3-1103	10.13
A 521	165	73.558	-10.273	4.944	0.2475	J0454.1-1014	12.97
A 2744	124	3.586	-30.352	4.964	0.3066	J0014.3-3023	19.79
A 1689	197	197.808	-1.337	15.332	0.1832	J1311.4-0120	23.59
1E 0657-56	566	104.751	-55.904	9.079	0.2965	J0658.5-5556	35.55
RX J1347-114	232	206.889	-11.734	6.468	0.4516	J1347.5-1144	63.43

Notes. ^(a) Most commonly used name of cluster or central object. ^(b) Combined ACIS-S/I exposure after excluding times of high background. ^(c) ROSAT 0.1–2.4 keV X-ray flux in 10⁻¹⁵ W/m². ^(d) ROSAT 0.1–2.4 keV X-ray luminosity in 10³⁷ W (REFLEX column: LumCor, *h* = 0.5).

Appendix B: *Chandra* datasets**Table B.1.** *Chandra* datasets used in this study.

Cluster ^a	<i>Chandra</i> ObsID ^b
1e0657	554, 3184, 4984, 4985, 4986, 5355, 5356, 5357, 5358, 5361
2a0335	919, 7939, 9792
3c348	1625, 5796, 6257
a1413	537, 1661, 5002, 5003, 7696
a1650	4178, 5822, 5823, 6356, 6357, 6358, 7242, 7691
a1689	540, 1663, 5004, 6930, 7289, 7701
a1775	12891, 13510
a1795	493, 494, 3666, 5286, 5287, 5288, 5289, 5290, 6159, 6160, 6161, 6162, 6163, 10432, 10433, 10898, 10899, 10900, 10901, 12026, 12027, 12028, 12029, 13106, 13107, 13108, 13109, 13110, 13111, 13112, 13113, 13412, 13413, 13414, 13415, 13416, 13417, 14268, 14269, 14270, 14271, 14272, 14273, 14274, 14275, 15485, 15486, 15487, 15488, 15489, 15490, 15491, 15492, 16432, 16433, 16434, 16435, 16436, 16437, 16438, 16439, 16465, 16466, 16467, 16468, 16469, 16470, 16471, 16472
a1835	495, 496, 6880, 6881, 7370
a1995	906, 7021, 7713
a2034	2204, 7695, 12885, 12886, 13192, 13193
a2052	890, 5807, 10477, 10478, 10479, 10480, 10879, 10914, 10915, 10916, 10917
a2146	10464, 10888, 12245, 12246, 12247, 13020, 13021, 13023, 13120, 13138
a2199	497, 498, 10748, 10803, 10804, 10805
a2204	499, 6104, 7940
a2390	500, 501, 4193
a2597	922, 6934, 7329, 15144
a2744	2212, 7712, 7915, 8477, 8557
a3667	513, 889, 5751, 5752, 5753, 6292, 6295, 6296, 7686
a401	518, 2309, 14024
a496	931, 3361, 4976
a520	528, 4215, 7703, 9424, 9425, 9426, 9430
a521	430, 901, 12880, 13190
a665	531, 3586, 7700, 12286, 13201, 15148
a907	535, 3185, 3205
cygnusa	360, 5830, 5831, 6225, 6226, 6228, 6229, 6250, 6252
hydraa	575, 576, 4969, 4970
ms0735	4197, 10468, 10469, 10470, 10471, 10822, 10918, 10922
ms1455	543, 4192, 7709
pks0745	508, 2427, 6103, 7694, 12881
rxj1347	506, 507, 3592, 13516, 13999, 14407
sersic159	1668, 11758
zw3146	909, 9371

Notes. ^(a) Abbreviated cluster name. ^(b) List of *Chandra* observations used in this study (indicated by their ObsID, observation identification number).

Appendix C: Perturbation table

Table C.1. Measured fractional perturbations.

Cluster ^a	dP ^b [per cent]	dS ^b [per cent]	dT ^b [per cent]	dn ^b [per cent]
1e0657	20.4 ^{+1.6} _{-1.4}	17.3 ^{+2.1} _{-1.5}	8.8 ^{+1.5} _{-1.4}	20.9 ^{+1.2} _{-0.9}
2a0335	11.7 ^{+0.6} _{-0.5}	19.8 ^{+0.9} _{-0.6}	9.3 ^{+0.5} _{-0.4}	13.5 ^{+0.6} _{-0.4}
3c348	1.3 ^{+2.9} _{-1.3}	12.0 ^{+1.9} _{-1.7}	3.6 ^{+2.0} _{-2.8}	8.5 ^{+0.9} _{-0.6}
a1413	5.4 ^{+1.9} _{-4.0}	6.4 ^{+2.8} _{-2.6}	0.3 ^{+2.4} _{-0.3}	8.7 ^{+1.0} _{-0.7}
a1650	5.5 ^{+0.9} _{-1.0}	14.0 ^{+1.0} _{-1.0}	4.0 ^{+1.0} _{-1.0}	10.0 ^{+0.7} _{-0.5}
a1689	0.6 ^{+2.7} _{-0.6}	1.1 ^{+2.8} _{-1.1}	0.8 ^{+2.1} _{-0.8}	3.8 ^{+0.4} _{-0.2}
a1775	0.6 ^{+3.5} _{-0.6}	20.7 ^{+2.6} _{-2.3}	12.6 ^{+1.9} _{-2.1}	8.0 ^{+0.8} _{-0.8}
a1795	5.3 ^{+0.2} _{-0.2}	22.3 ^{+0.5} _{-0.2}	11.7 ^{+0.4} _{-0.1}	12.4 ^{+0.3} _{-0.1}
a1835	6.0 ^{+1.1} _{-1.1}	15.8 ^{+1.5} _{-1.1}	9.3 ^{+1.0} _{-0.8}	8.8 ^{+0.6} _{-0.5}
a1995	5.7 ^{+5.5} _{-5.7}	13.6 ^{+4.9} _{-3.5}	11.4 ^{+3.7} _{-5.8}	7.0 ^{+1.6} _{-0.9}
a2034	12.8 ^{+2.2} _{-1.7}	6.5 ^{+2.1} _{-2.4}	6.1 ^{+1.6} _{-3.4}	9.1 ^{+1.0} _{-0.7}
a2052	7.5 ^{+0.2} _{-0.2}	18.3 ^{+0.6} _{-0.4}	11.6 ^{+0.4} _{-0.2}	10.1 ^{+0.3} _{-0.2}
a2146	20.3 ^{+1.9} _{-1.9}	37.1 ^{+4.1} _{-3.2}	12.2 ^{+1.7} _{-1.4}	24.3 ^{+2.7} _{-1.5}
a2199	7.6 ^{+0.4} _{-0.3}	13.2 ^{+0.6} _{-0.4}	7.3 ^{+0.4} _{-0.3}	8.6 ^{+0.3} _{-0.3}
a2204	6.7 ^{+1.2} _{-1.3}	13.7 ^{+1.7} _{-1.0}	8.7 ^{+1.1} _{-1.0}	7.6 ^{+0.5} _{-0.5}
a2390	11.4 ^{+2.0} _{-1.8}	19.0 ^{+2.6} _{-1.9}	12.4 ^{+2.1} _{-2.0}	11.2 ^{+1.1} _{-0.8}
a2597	8.1 ^{+0.8} _{-0.6}	8.9 ^{+0.8} _{-0.6}	5.5 ^{+0.6} _{-0.6}	7.2 ^{+0.5} _{-0.4}
a2744	9.8 ^{+4.2} _{-9.8}	13.4 ^{+3.1} _{-2.7}	7.6 ^{+3.5} _{-7.6}	15.1 ^{+1.4} _{-1.1}
a3667	24.6 ^{+1.1} _{-1.1}	12.4 ^{+0.7} _{-0.5}	16.1 ^{+0.9} _{-0.7}	11.4 ^{+0.5} _{-0.4}
a401	6.1 ^{+1.3} _{-1.5}	8.1 ^{+1.0} _{-1.3}	2.8 ^{+1.3} _{-2.8}	7.5 ^{+0.5} _{-0.3}
a496	9.0 ^{+0.6} _{-0.6}	21.7 ^{+1.2} _{-1.0}	14.0 ^{+0.9} _{-0.6}	8.9 ^{+0.5} _{-0.4}
a520	12.6 ^{+2.0} _{-1.8}	15.0 ^{+2.6} _{-1.4}	7.6 ^{+1.9} _{-1.7}	11.5 ^{+1.4} _{-0.9}
a521	12.1 ^{+5.3} _{-7.8}	16.7 ^{+8.2} _{-7.2}	10.0 ^{+6.4} _{-8.0}	10.7 ^{+2.3} _{-1.4}
a665	11.8 ^{+2.4} _{-2.4}	8.2 ^{+2.6} _{-4.6}	6.5 ^{+2.6} _{-3.9}	11.0 ^{+0.9} _{-0.8}
a907	0.2 ^{+2.4} _{-0.2}	12.1 ^{+1.9} _{-1.7}	1.7 ^{+2.9} _{-1.7}	9.5 ^{+0.9} _{-0.6}
cygnusa	18.2 ^{+1.0} _{-0.8}	23.4 ^{+1.3} _{-1.0}	14.1 ^{+0.8} _{-0.6}	27.3 ^{+1.2} _{-0.9}
hydraa	9.8 ^{+0.4} _{-0.3}	14.4 ^{+0.6} _{-0.5}	9.7 ^{+0.4} _{-0.3}	7.8 ^{+0.3} _{-0.2}
ms0735	10.6 ^{+1.5} _{-0.9}	14.0 ^{+1.7} _{-1.2}	7.8 ^{+1.2} _{-0.8}	10.3 ^{+1.0} _{-0.7}
ms1455	4.1 ^{+2.0} _{-3.5}	19.0 ^{+2.6} _{-1.9}	9.0 ^{+2.0} _{-1.5}	11.1 ^{+1.0} _{-0.8}
pks0745	3.4 ^{+1.0} _{-1.9}	19.0 ^{+1.0} _{-0.8}	9.4 ^{+0.8} _{-0.6}	11.6 ^{+0.4} _{-0.5}
rxj1347	13.4 ^{+2.3} _{-2.3}	23.4 ^{+3.3} _{-2.1}	16.0 ^{+2.3} _{-2.0}	13.8 ^{+1.5} _{-0.8}
seraic159	9.7 ^{+1.1} _{-0.7}	11.4 ^{+1.1} _{-1.1}	5.2 ^{+0.6} _{-0.6}	9.2 ^{+0.9} _{-0.5}
zw3146	0.4 ^{+2.3} _{-0.4}	25.9 ^{+2.5} _{-2.2}	10.9 ^{+1.9} _{-1.9}	15.9 ^{+1.3} _{-0.9}

Notes. ^(a) Abbreviated cluster name. ^(b) Measured average fractional spread of thermodynamic properties for the whole cluster (see Sect. 3.1, $M = 1$) in per cent.

Appendix D: 2D Maps

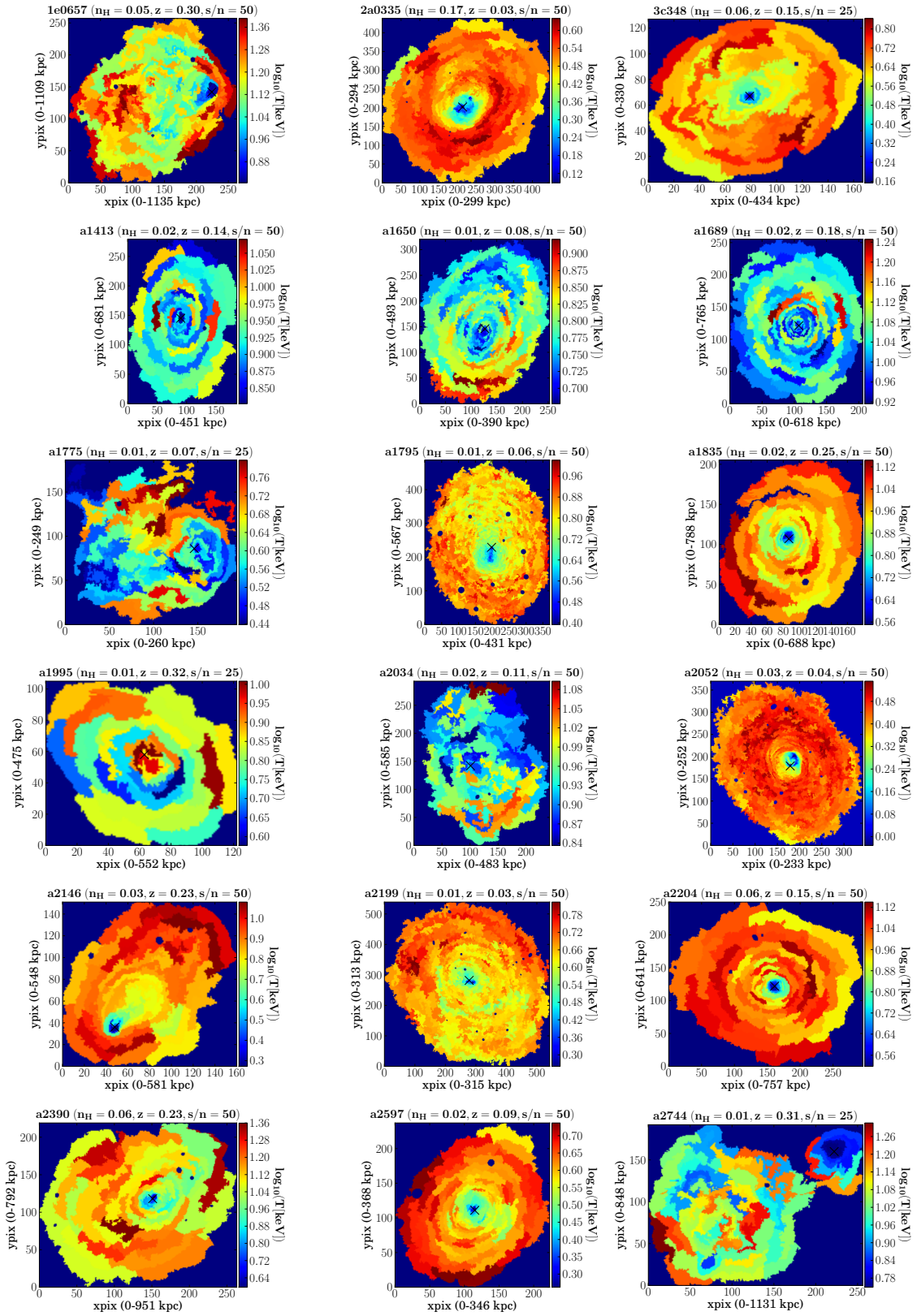


Fig. D.1. Temperature maps of all clusters in the sample. Bins have a S/N of 50 or 25 (see Sect. 3.1) and temperatures are shown on a logarithmic colour scale. Excluding areas below the surface brightness cut (area-normalised normalisation $>10^{-7} \text{ cm}^{-5} \text{ arcsec}^{-2}$) and where the errors on temperature are more than twice the best-fit temperature value. The plot title gives the abbreviated cluster name, the average foreground column density n_H [cm^{-2}], and the redshift z . Scale: 1 pix $\sim 1''$. Crosses denote the peak of X-ray emission.

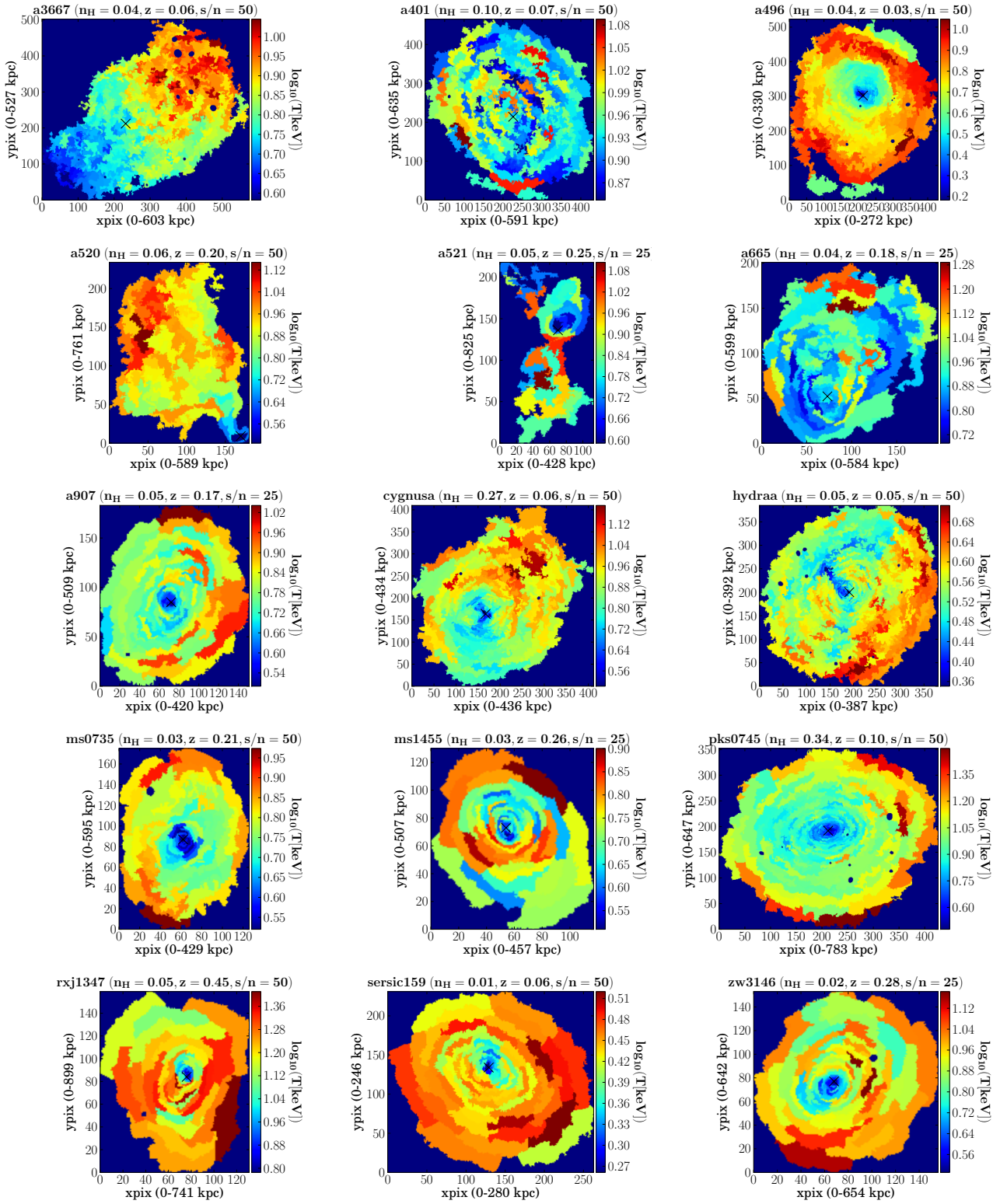


Fig. D.1. continued.

Appendix E: Unsharp-masked count images

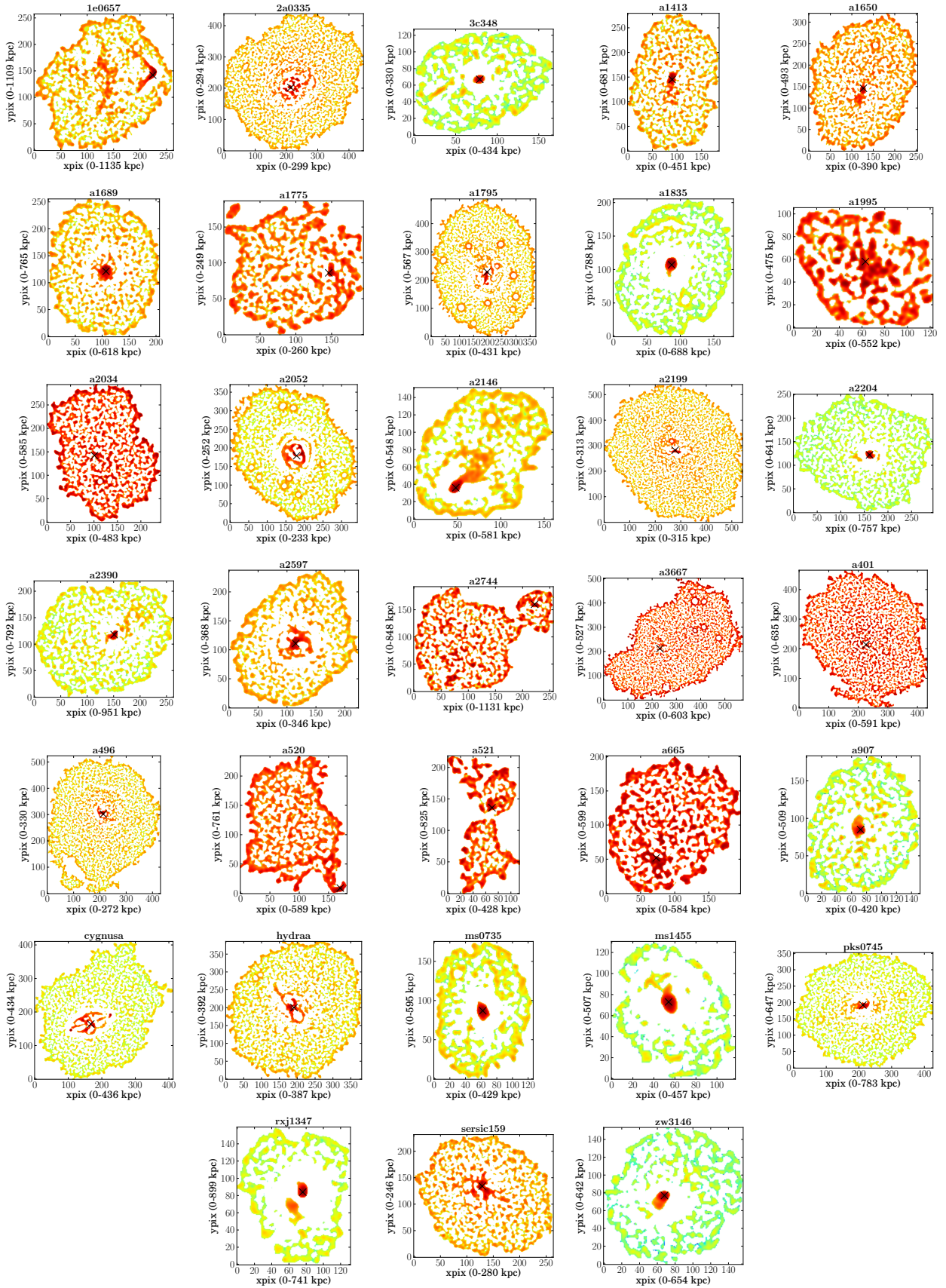


Fig. E.1. Unsharp-masked exposure-corrected images (logarithmic colour scale) of all clusters in the sample showing the difference between two count images smoothed with a Gaussian function (2 pixels and 5 pixels sigma). Colours indicate relative surface brightness differences (over-densities dark red, under-dense areas green to white). Scale: 1 pix \sim 1". Crosses mark the peak of the X-ray emission.

Appendix F: Projected radial profiles

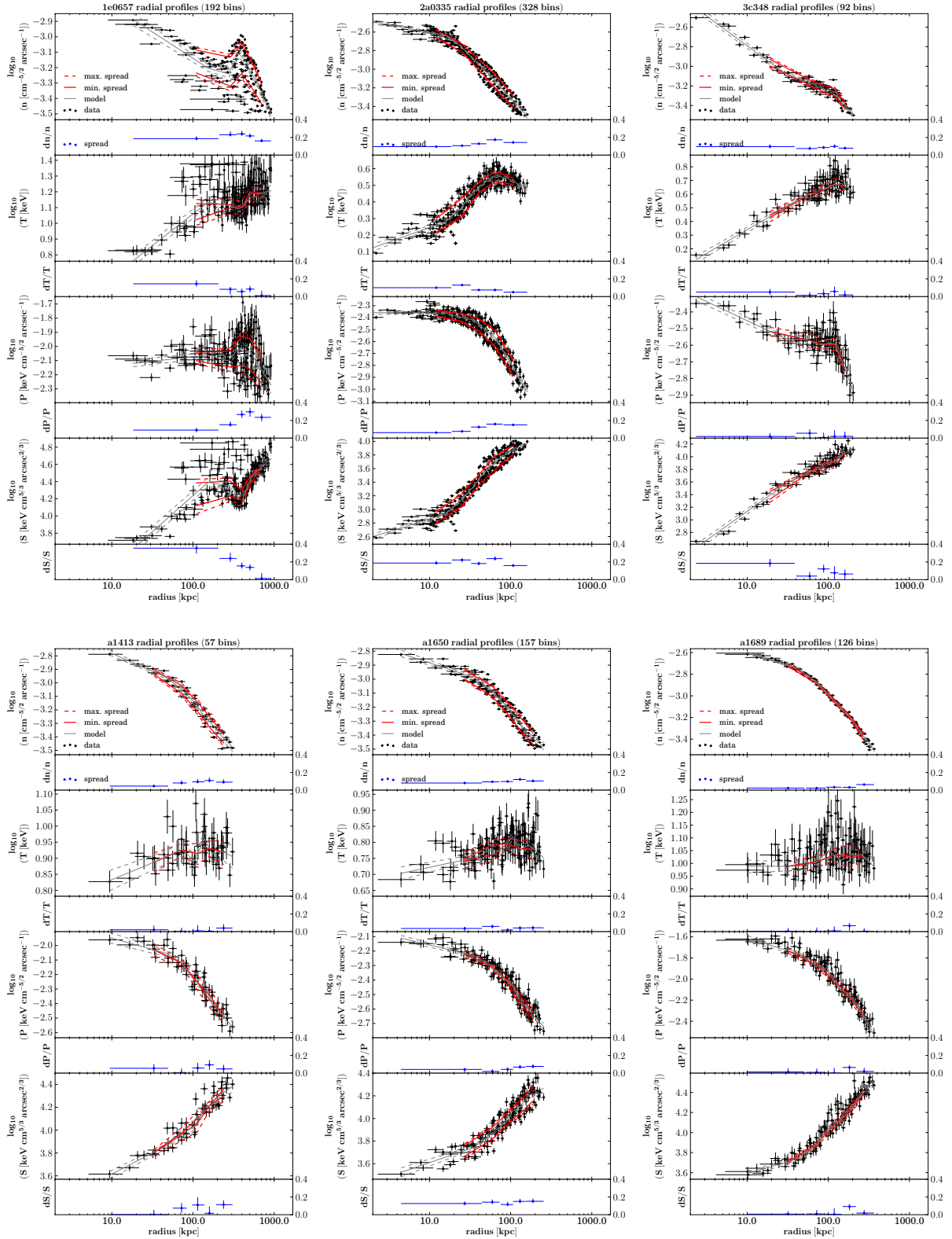


Fig. F.1. Radial profiles of projected density, temperature, pressure, and entropy. Cluster names are given in the plot titles. The cluster centres are marked as crosses in Figs. D.1 and E.1. Error bars are the fit errors and the standard deviation of the radial distribution for all spatial-spectral bins. The plotted lines show limits on intrinsic scatter around an average seven-node model (grey lines) within the given radial range (see Sect. 3.1). The small panels show the measured fractional scatter ($M = 5$) with confidence and radial range.

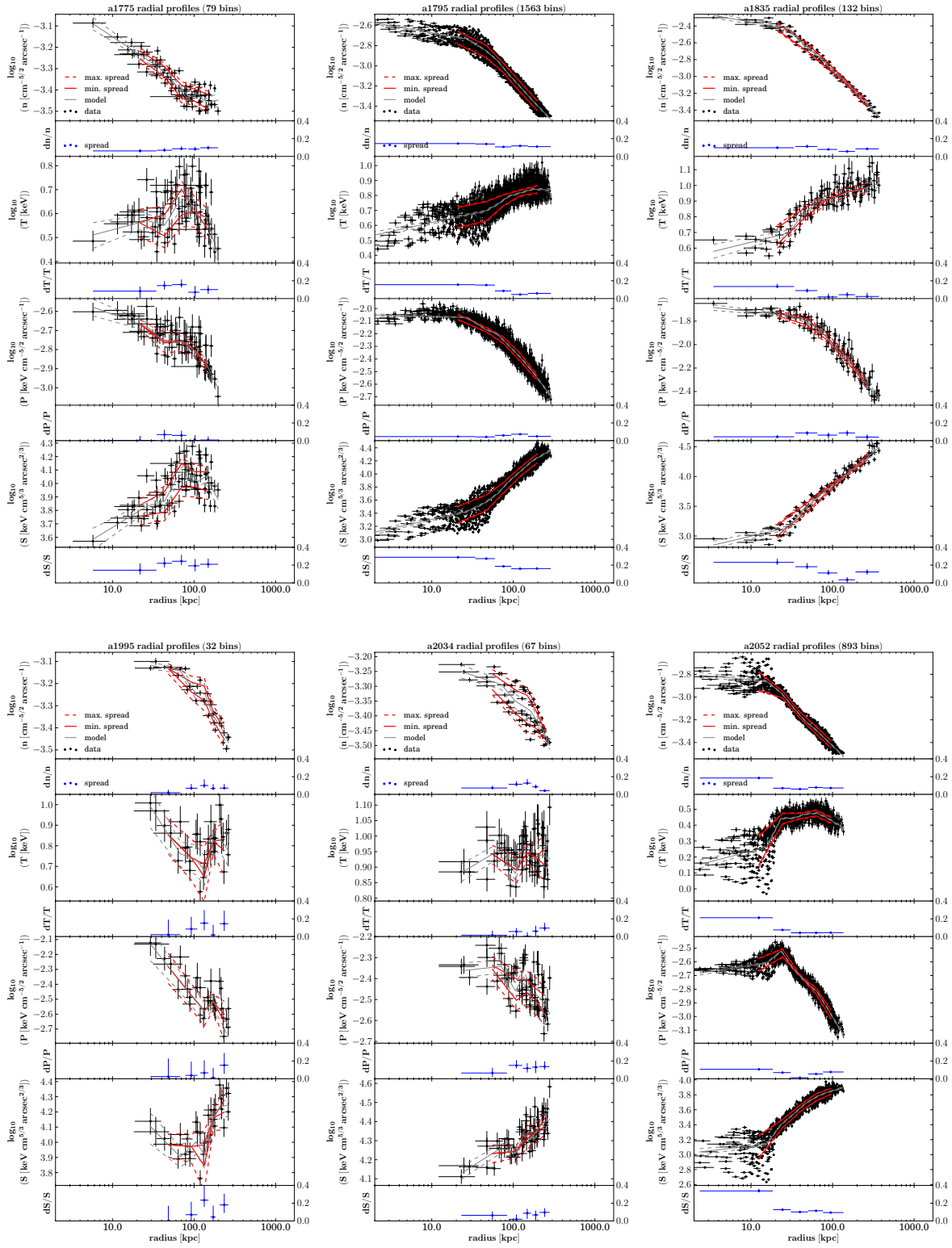


Fig. F.1. continued.

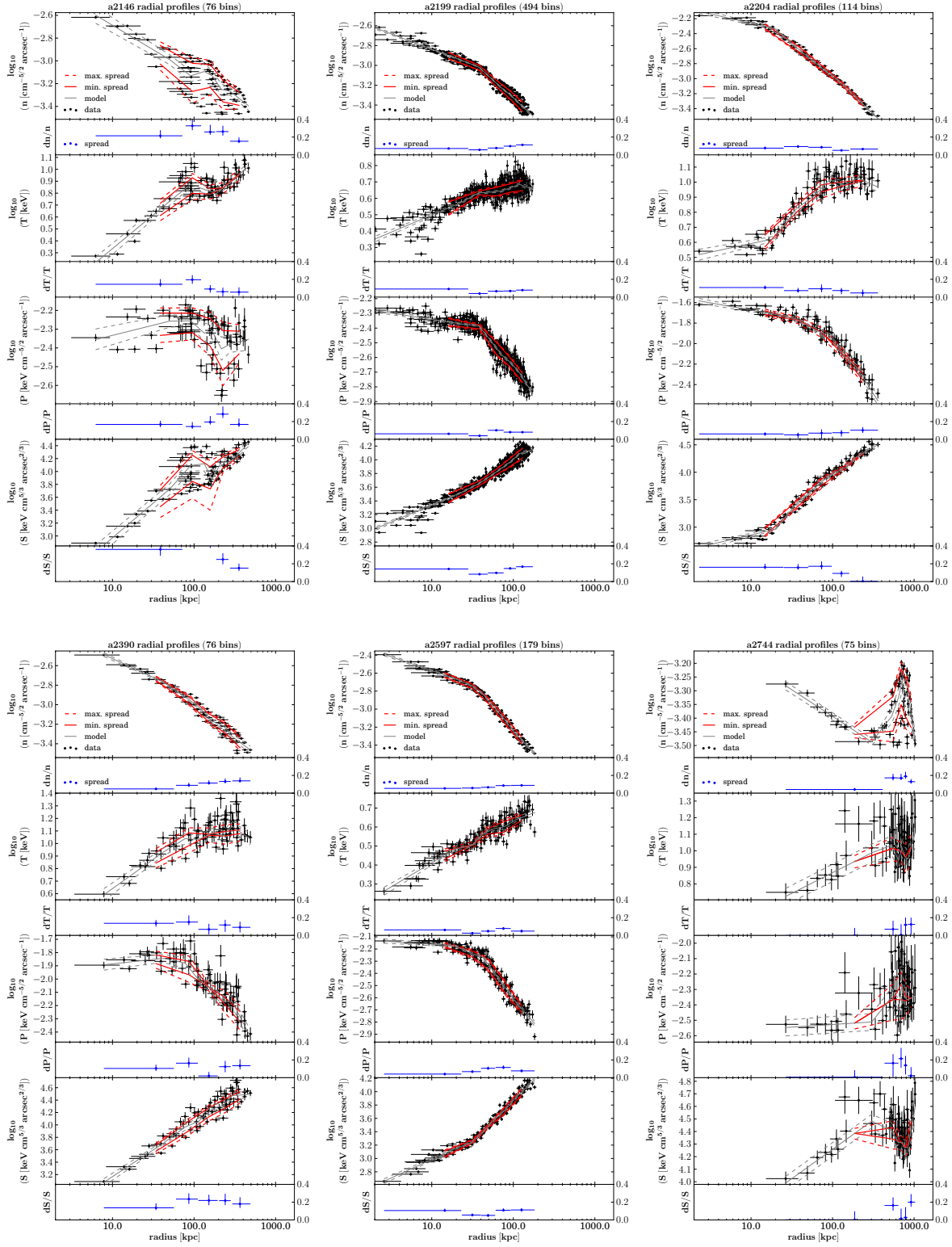


Fig. F.1. continued.

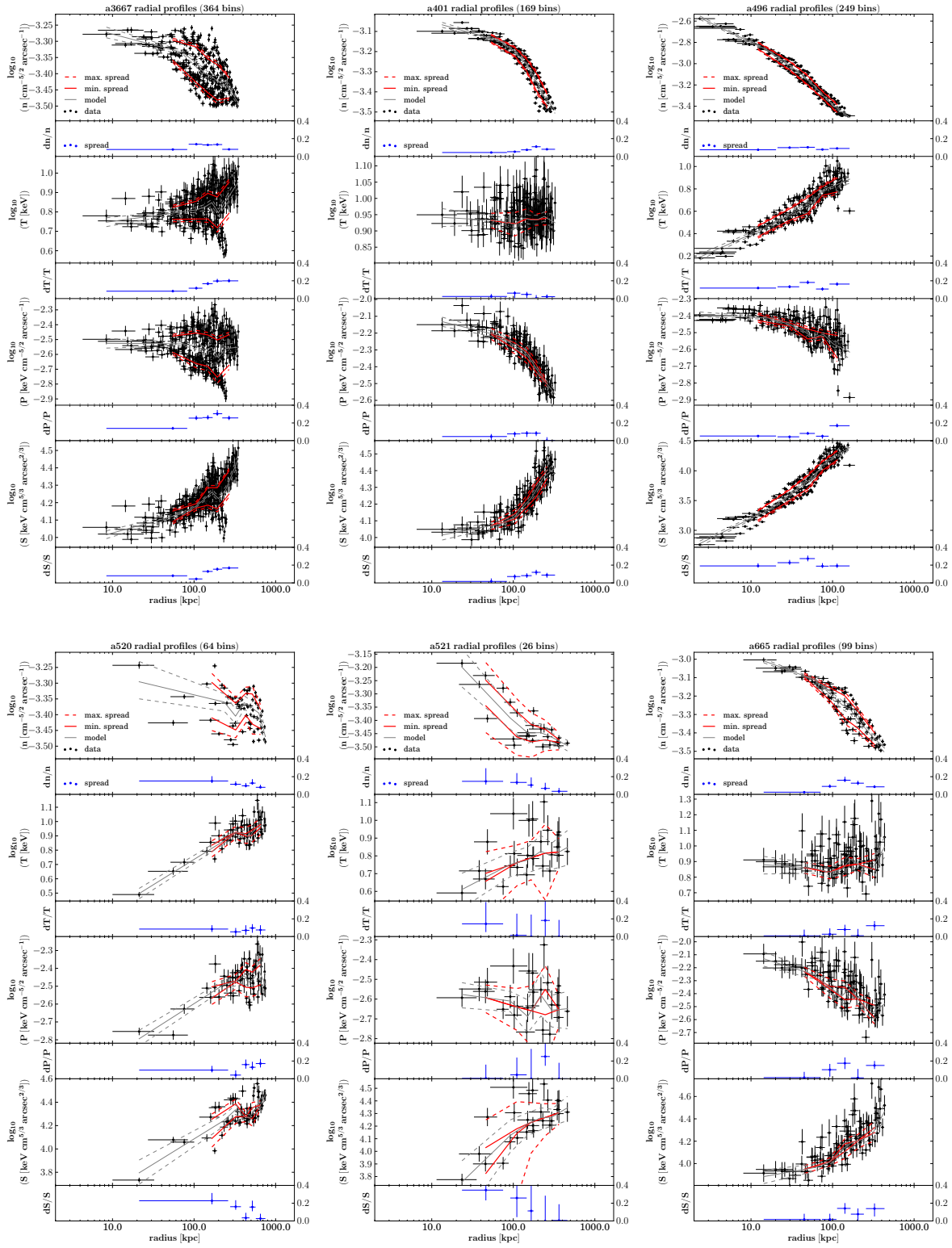


Fig. F.1. continued.

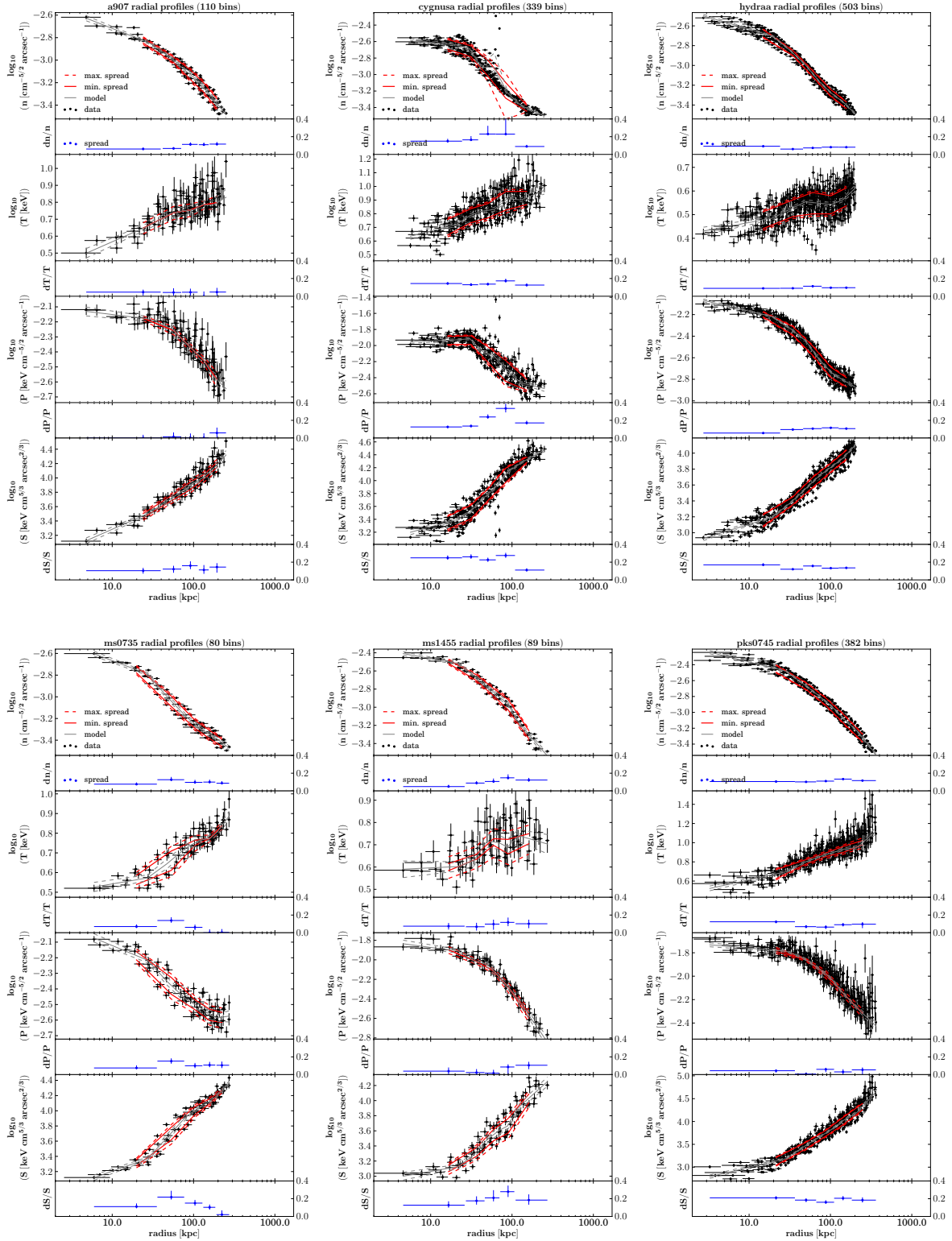


Fig. F.1. continued.

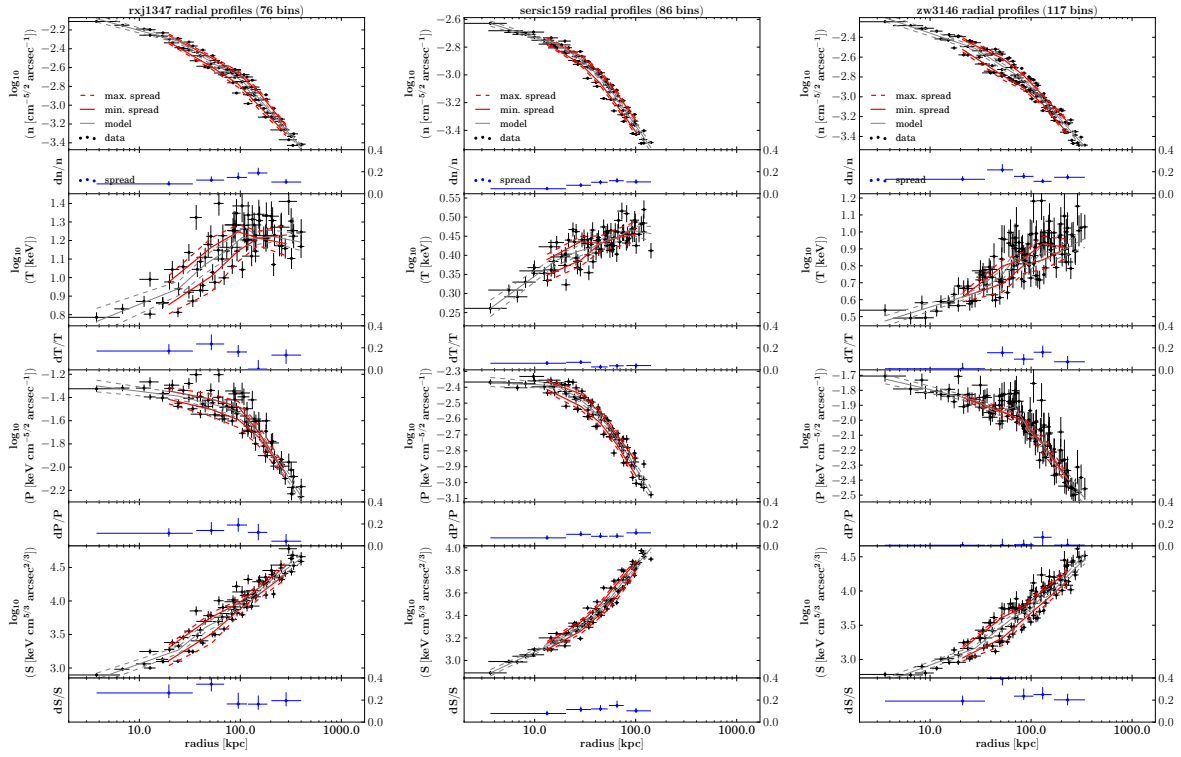


Fig. F.1. continued.